Study of Wall-Thermal Effects on Lean Premixed Hydrogen Combustion

Harshit Sabharwal

Delft University of Technology

TU Delft

Study of Wall-Thermal Effects on Lean Premixed Hydrogen Combustion

by

Harshit Sabharwal

to obtain the degree of **Master of Science**
at the Delft University of Technology,
to be defended publicly on 12th December 2025.

Student Number:	6054056	
Project Duration:	April 2025 - December 2025	
Thesis Committee:	Dr. A.M.J. Felden	Supervisor, TU Delft
	Prof.dr.ir. S.A. Klein	Supervisor, TU Delft
	Dr. P. Simões Costa	TU Delft

TU Delft

Abstract

For centuries, combustion has played an important role in human development, yet as Giusti and Mastorakos notes [29], ”with some 100,000 years of development, combustion might be expected to be a mature technology. In fact, it is the least developed technology of modern engineering systems”. As the world transitions away from carbon based fuels, hydrogen has emerged as a promising alternative due to its carbon free combustion. However, replacing conventional fuels with hydrogen introduces significant technical challenges. Pure hydrogen–air flames exhibit high laminar flame speeds and low ignition energies, making combustor hardware more susceptible to flame flashback. Flashback not only disrupts stable operation but can also result in damage and system failures. A thorough understanding of flame stabilization and flashback mechanisms is therefore essential.

In this context, the present work investigates a combustor geometry designed to generate a trapped vortex, a recirculation zone that enhances flame stabilization. Accurate numerical predictions of such phenomena requires realistic thermal boundary conditions, yet these are often unavailable in experimental configurations and are commonly oversimplified in simulations. This study evaluates how different thermal wall boundary conditions modify flame stability and flow behavior in a premixed pure hydrogen–air trapped vortex combustor at lean conditions. A 2D and 3D simplified version of the FlameSheet™ burner, originally developed by Power Systems Manufacturing (PSM), is modeled in this study, using PeleLMeX [24].

The study begins with a 2D cold flow simulation performed using DNS. This computation is analyzed in light of a previously performed 3D study of the same geometry, with the same numerical solver and following the same numerical approach [25]. Differences are acknowledged and explained. After examining the baseline flow behavior, six reactive cases are then simulated, varying the main flow Reynolds number (12,000 and 8,000) and the thermal boundary conditions applied to the liner walls (adiabatic, isothermal at 300 K, and a fitted temperature profile based on experimental data). Results show that wall thermal conditions significantly affect flame stability and structure. Time averaged fields reveal that thermal boundary conditions also influence recirculation zone size and peak flame temperatures. The 2D simulations, while limited in capturing full 3D turbulence, offer valuable insights into flame wall interactions and highlight the importance of accurate thermal boundary conditions in predicting flashback propensity and flame stabilization in hydrogen combustors.

Acknowledgment

I would like to express my sincere gratitude to everyone who supported and guided me during this master's thesis.

First and foremost, I am deeply thankful to my supervisor, Dr. Anna Felden, for her continuous guidance, constructive feedback, and encouragement throughout this project and Dr. Sikke Klein for taking time to help me out with questions and providing guidance. I am especially grateful to Anna for her patient supervision, valuable input on numerical modeling, and detailed feedback that significantly improved the quality of this work. Her guidance and structured approach also helped me manage my workload effectively throughout the thesis. Their expertise and motivation made this thesis both a challenging and rewarding experience.

I would also like to thank Dr. Mathieu Pourquie for providing access to computational resources and to Dr. Pedro Simões Costa for being part of my graduation committee. I am also grateful to Rafael Pichler and Tarun Hegde for the discussions, encouragement, and good company throughout this journey.

Finally, I am grateful to my family and friends for their constant love, patience, and support from afar. Their belief in me has been a steady source of strength during both the demanding and rewarding moments of this work.

Thank you all for being part of this journey.

Harshit Sabharwal
Delft, December 2025

Contents

Nomenclature

Abbreviations

Abbreviation	Definition
BC	Boundary Condition
CFD	Computational Fluid Dynamics
CFL	Courant–Friedrichs-Lewy condition
DNS	Direct Numerical Simulation
AMR	Adaptive Mesh Refinement
EBs	Embedded Boundaries
FVM	Finite Volume Method
GHGs	Greenhouse Gases
LES	Large Eddy Simulation
N–S	Navier–Stokes
RANS	Reynolds Averaged Navier-Stokes
TKE	Turbulent Kinetic Energy

Symbols

Symbol	Definition	Unit
V	Velocity	[m/s]
ρ	Density	[kg/m^3]
u, v, w	Velocity components in x, y, and z directions	[m/s]
T	Temperature	[K]
p	Pressure	[Pa]
Y_k	Mass fraction of species k	[-]
$\dot{\omega}_k$	Reaction rate of species k	[kg/(m^{3}s)]
μ	Dynamic viscosity	[Pa·s]
ν	Kinematic viscosity	[m^2/s]
λ	Thermal conductivity	[W/(m·K)]
S_L	Laminar flame speed	[m/s]
δ_L	Laminar flame thickness	[m]
ϕ	Equivalence ratio	[-]
ε	Dissipation rate of turbulent kinetic energy	[m^2/s^3]
u'	RMS velocity fluctuation	[m/s]
l_0	Integral length scale	[m]
D	Diffusion coefficient	[m^2/s]
E_j	Activation energy	[J/mol]
R	Universal gas constant	[J/(mol·K)]
Δh_f°	Standard enthalpy of formation	[J/mol]
κ	von Kármán constant	[-]
t	Time	[s]
x, y, z	Spatial coordinates	[m]
Q	Heat release rate	[W]
τ_{ij}	Stress tensor component	[Pa]
t_{pp}	Acquisition time step	[s]
t_{sample}	Sampling interval	[s]

1

Introduction

The increasing global demand for energy, coupled with the urgent need to mitigate climate change, has intensified the search for sustainable and cleaner fuel alternatives. Fossil fuels, which have powered industries and economies for more than a century, are major contributors to carbon dioxide (CO_2) emissions, leading to global warming and severe environmental consequences. Rising temperatures, extreme weather events, and shrinking ice caps underscore the need to transition to energy sources that reduce greenhouse gas emissions.

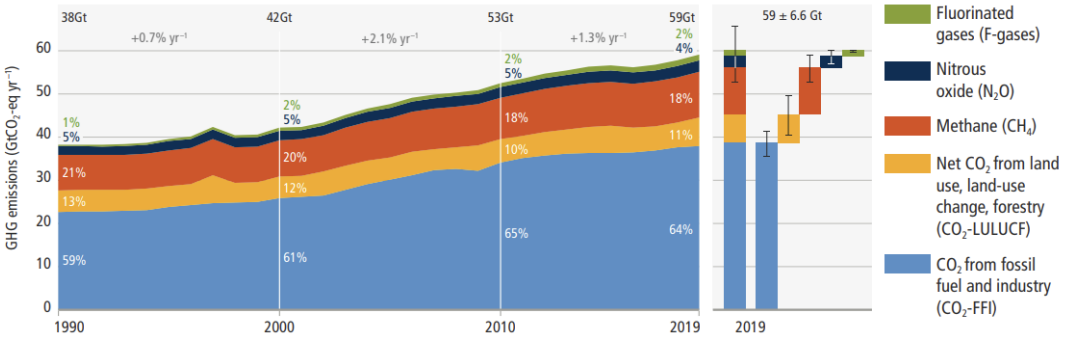

Figure 1.1: Trends in global GHG emissions by sector [16]

Figure 1.1 we can see that growth in emissions has persisted across all major groups of GHGs since 1990. By 2019, the largest growth in absolute emissions occurred in CO_2 from fossil fuel combustion and other industrial processes followed by CH_4. The Paris Agreement [80], adopted in 2015, set ambitious targets to limit global temperature rise to well below 2°C above pre-industrial levels, with an aspiration to restrict it to 1.5°C as seen in Fig. 1.2 (discussed below). Achieving this goal requires a drastic reduction in carbon emissions across all sectors: energy (fossil fuel-based power generation), transport (road, aviation, shipping), industry (cement, steel, chemicals), buildings (heating/cooling), agriculture and land use (deforestation, livestock). Governments and industries worldwide are now prioritizing decarbonization strategies, with H_2 emerging as a key component of the clean energy transition as a low carbon energy carrier [16].

More recently at COP28, the 28th annual United Nations climate meeting held in Dubai, UAE, world leaders reaffirmed the urgency of reducing fossil fuel dependency [79]. In a landmark agreement, parties recognized the need to ”transition away from fossil fuels in energy systems” in a just and equitable manner. This commitment signals a global shift toward renewable energy sources, including hydrogen, which is viewed as a key player in the path to net-zero emissions [78].

Figure 1.2 provides a visual summary of projected global temperature increases by the year 2100 under different scenarios. Without any policies (the ”Baseline” curve), global warming could reach +4.1–4.8°C, while current policies (as of 2018) would lead to +3.1–3.5°C as existing measures like limited renewable subsidies and regional carbon pricing remain insufficient without global fossil fuel phase-outs. If all announced but unimplemented policies including coal bans in OECD (Organisation for Economic Co-operation and Development) nations by 2030, which are a group of 38 high income market economy countries, EV mandates, and ending direct fossil fuel subsidies though gaps persist in methane reduction and deforestation are enacted (the optimistic policies curve), warming could be limited to +3.0°C. The government pledges from various countries under the Paris Agreement might restrict global warming to +2.7–3.0°C, but this still falls short of the Agreement's goals. To align with the ”well below 2°C” target, systemic changes are needed: no new coal plants (with retirement by 2040), green hydrogen for heavy industry, circular economy mandates, and binding deforestation bans by 2030, all backed by carbon pricing. Achieving the 1.5°C goal requires additional emergency actions: 100% clean electricity by 2035–2040, scaling negative emissions technologies like carbon capture and storage, absolute transport demand reductions, synthetic fuels for aviation/shipping, and a global carbon price of $100–200/ton by 2030—coupled with bans on new oil/gas projects [15].

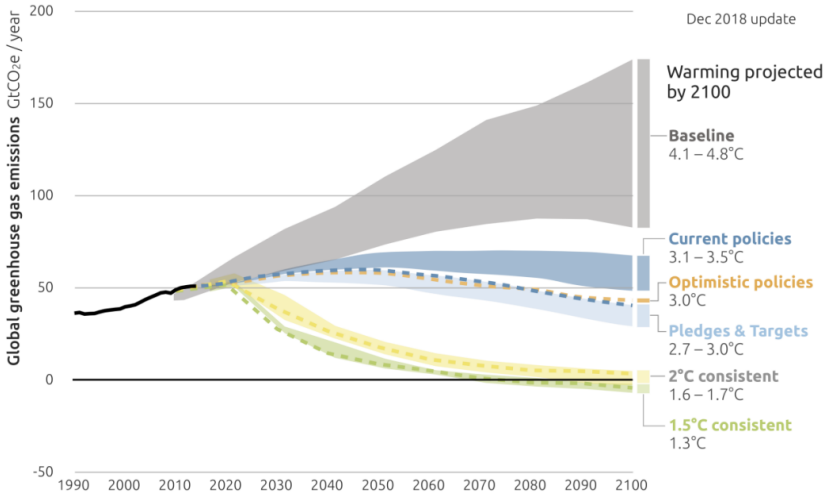

Figure 1.2: Expected global temperature increase by the end of the century compared to pre-industrial levels implied by global emissions pathways in 6 scenarios [15]

Amongst the various renewable energy sources, solar and wind power have gained substantial interest due to their ability to produce clean energy with near-zero emissions. However, these sources are associated with high production, installation and maintenance costs. Another major drawback of these sources is their inherent intermittency—a dependence on variable weather conditions that leads to fluctuations in power [35]. This variability makes them unreliable as standalone energy solutions. To address this issue, energy storage systems or complementary power sources are essential. Technologies such as battery storage, hydrogen production, and pumped hydro storage are emerging as viable solutions to bridge the gap between energy production and consumption.

Hydrogen is playing an important role in supporting the decarbonization of various sectors, e.g. industry, transport or power generation [84]. Globally, the industry already produces and uses H_2 on a massive scale. A plethora of catalysts and catalytic processes involving hydrogen have been developed, ranging from the synthesis of ammonia to the production pharmaceuticals [54]. Significant research efforts are focused on integrating H_2 across four critical areas of the energy sector: (1) production via renewable-powered electrolysis, (2) re-electrification using fuel cells or hydrogen turbines, and (3) storage in geological formations or high-pressure systems [84], and (4) direct use as a clean fuel in industrial processes and combustion applications. Hydrogen is particularly promising for long duration energy storage, as it enables seasonal retention of surplus renewable electricity. This capability helps stabilize grid supply during extended periods of low generation (e.g., winter months with

reduced solar irradiance) [81].

Investigating hydrogen combustion is of practical importance due to two main reasons: power generation and safety. Hydrogen as a fuel has gained significant attention due to its potential as a clean and sustainable energy source, when used in combustion processes or fuel cells, because it produces water as the primary byproduct, resulting in minimal environmental impact and near zero greenhouse gas emissions. Hydrogen has higher adiabatic flame temperature, higher speed of flame propagation, low molecular weight, and consequently a higher diffusion rate and reactivity when compared to conventional fuels like methane [70]. Along with these properties there are many problems for a traditional burner to make use of hydrogen rich fuels such as flame flashback, blowout, local high temperatures, auto ignition and high NO_x emissions [69]. These tradeoffs underscore the need for careful engineering in hydrogen-based energy systems. Conventional gas turbine burners are not designed to handle high flashback propensity of hydrogen-air mixtures. Therefore novel burners need to be conceptualized and developed. One such burner is FlameSheet™ burner [74, 75], and the primary objective of this thesis is detailed investigation and characterization of its flow field when operated with premixed hydrogen–air mixtures at a low equivalence ratio.

1.1. Flame Flashback

1.1.1. Flame Flashback Mechanisms

Flame flashback represents one of the most critical safety challenges in hydrogen combustion systems. This phenomenon occurs when the flame propagates upstream into the premixing zone, contrary to its designed downstream path, potentially causing damage to combustion hardware. Hydrogen's unique properties - including a high diffusivity, wide flammability range, and low minimum ignition energy; make it particularly susceptible to flashback compared to other hydrocarbon fuels [39]. Flashback can occur as a result of at least four different mechanisms [52]. Each of them are introduced briefly for context.

- **Core Flow Flashback**
  Flame propagation in the combustor takes place when the turbulent burning velocity exceeds the local flow velocity in the core flow, either due to deceleration, transients (like startup or shutdown), or flow instabilities. Turbulent burning velocity which is a function of turbulent flame interaction and chemical kinetics plays an important role in triggering core flow flashback.
- **Combustion Instability Induced Flashback**
  Flashback occurs due to large amplitude fluctuation in the flow field. Instabilities are caused by oscillations in pressure and heat release that occur in combustors, particularly in lean premixed combustion systems like gas turbines or rocket engines. These instabilities can induce flame movement and generate vortices leading to flow reversal, as seen in Fig. 1.3.
- **Combustion-Induced Vortex Breakdown (CIVB)**
  A more complex and important mechanism for swirl stabilized combustor is combustion induced vortex breakdown. Vortex breakdown is a unique characteristic of swirling flows. Strong swirling flows create a central recirculation zone (CRZ) that stabilizes the flame. However under certain conditions the central vortex can breakdown causing abrupt change in vortex structure leading to formation of a stagnation point and recirculation region downstream of it which can lead to upstream flame propagation as seen in Figure 1.4.

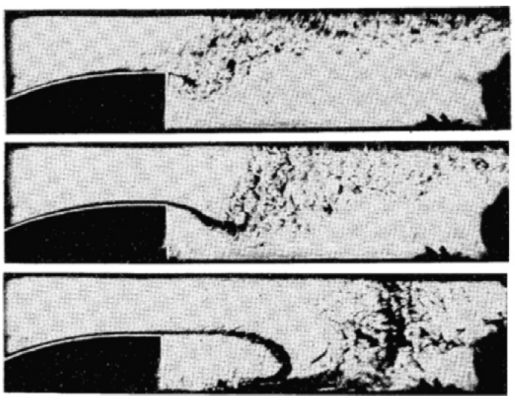

Figure 1.3: Combustion instability of a backward-facing step [39]

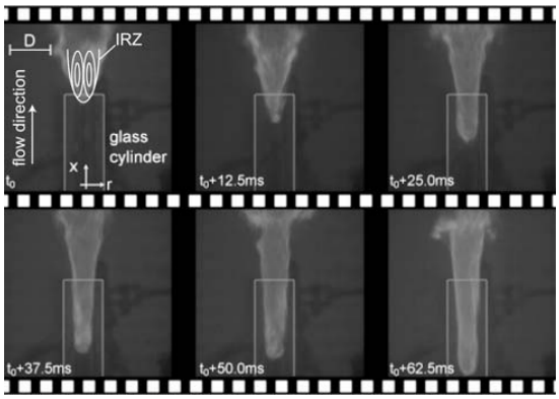

Figure 1.4: Flame propagation during a CIVB driven flashback [42]

- **Boundary Layer (BL) Flashback**
  Boundary layer flashback has been studied extensively in the literature and is considered as the primary mechanism for flashback. Flashback occurs at a location where the local burning velocity is greater than the local flow velocity near the walls. The flow velocity near the wall decreases because of no-slip boundary condition resulting in upstream flame propagation along the wall of a burner or premixer.

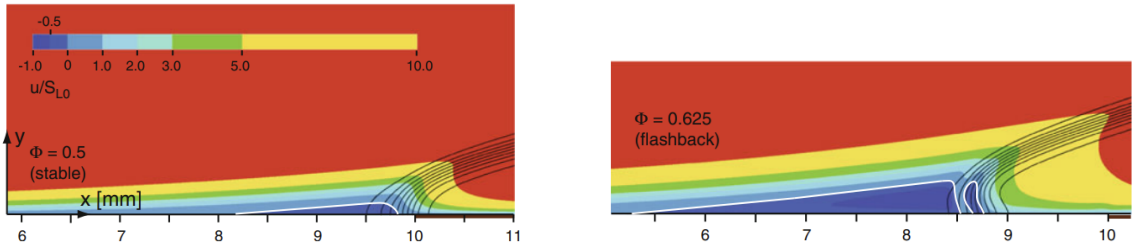

Figure 1.5: Axial velocity contour for the laminar premixed flame at stable and flashback condition[22]

As can be seen in Figure 1.5, as the maximum height of the backflow region reaches a certain value, which is dictated by energy balance, the reaction can sustain itself inside the backflow region, and flashback occurs. The backflow region, at the onset of flashback, is continuously moved upstream by the adverse pressure in front of the flame. This type of flashback mechanism is very relevant in our work, and we will focus on boundary layer flashback and not discuss the other mechanisms further.

1.1.2. Boundary Layer Flashback Modeling

The first model to predict boundary layer flashback in non-swirling premixed laminar flames was proposed by Lewis and von Elbe [50] in 1943, while Edse studied the turbulent boundary layer flashback at high pressure [21]. The Critical Velocity Gradient model suggests that flashback occurs when the velocity gradient near the burner's wall is too low to prevent the flame from propagating upstream.

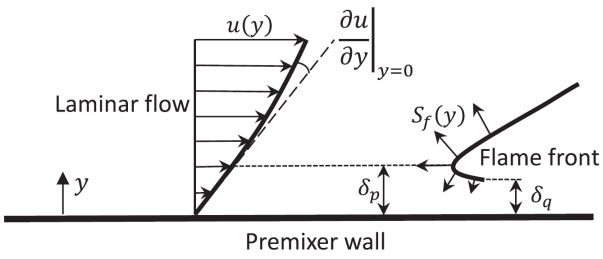

Figure 1.6: Schematic of CVG model[39]

Here the velocity profile of the unburned mixture $u(y)$ represents a laminar flow approaching the flame front. The flame speed denoted by $S_f(y)$ decreases near the wall due to quenching, and the quenching distance is denoted by δ_q. The velocity gradient at the wall is approximated by the ratio of the flow velocity to the penetration distance. This is based on the assumption that the flow velocity remains linear close to the wall.

$$g = \left|\frac{\partial u}{\partial y}\right| = \frac{|\tau_w|}{\mu_u}, \quad g_c = \frac{S_L}{\delta_p}, \quad \text{Flashback occurs when } g_c > g$$

However, the original model neglects flame-flow interaction. The flame strongly curves towards the unburned mixture as flame propagates upstream leading to a divergence of streamlines and adverse pressure gradient [39]. Later this model was extended to turbulent conditions [33, 34].

Since these early flashback studies, numerous investigations have been reported in the literature regarding the effect of fuel composition [19], flame confinement, and tip temperature [19, 20]. It was found that flame confinement substantially increases the risk of boundary layer flashback. For moderate enclosure sizes, this is mainly caused by increasing burner tip temperatures. The effect of pressure has been studied experimentally by [17, 41, 40].

To address the turbulent conditions, researchers have developed empirical correlations. University of California Irvine developed a Damkholer based correlation utilizing experimental data available at elevated pressures and temperatures. Alternatively, the ”flame angle theory” developed at Technische Universität München (TUM) provides a more physically grounded approach by modeling the flame interaction with the boundary layer. This method has been validated across a range of operating conditions and offers broader applicability [38].

Recent advances have focused on high fidelity modeling to capture the dynamics of BL flashback using LES [23] and DNS have been utilized to explore flame self-interaction (FSI) during turbulent BL flashback in hydrogen-rich premixed combustion. Understanding these interactions is crucial for developing accurate predictive models for BL flashback [1].

1.2. The FlameSheet™ Burner

The concept of trapped vortex burner (TVC) has attracted research for more than 20 years. It is an advanced concept in combustor design [70], which is receiving great interest due to improved flame stability and combustion efficiency, simple design, small pressure loss and reduced NO_x emissions [68]. In addition, the trapped vortex mechanism increases the combustor’s resistance to flame flashback which makes it a good candidate to be used with hydrogen fuel.

The FlameSheet™ combustor, developed by Power Systems Manufacturing (PSM) [74, 75, 65] is a two stage radially inflow ”combustor within a combustor”, where the inner stage is called the pilot combustor and the outer stage is called the main combustor. It was initially engineered to increase the operational

and fuel flexibility of land-based gas turbines running on natural gas, but it has also shown an excellent combustion performance with high hydrogen content fuels [35]. Figure 1.7 shows a schematic of the FlameSheet™ combustor. The pressurized air (blue arrows) enters the burner around its circumference and splits into two streams. The outer air stream leads to the pilot combustor and once properly mixed (red arrows) enters the combustor. The inner air stream takes the shorter path which includes the 180-degree turn which is the key feature of the design and creates a trapped vortex making the burner more resistant to flame flashback by disturbing the turbulent boundary layer. At high loads both combustors are used, with the outer combustor flame structure looking like a sheet of flame around the inner combustor.

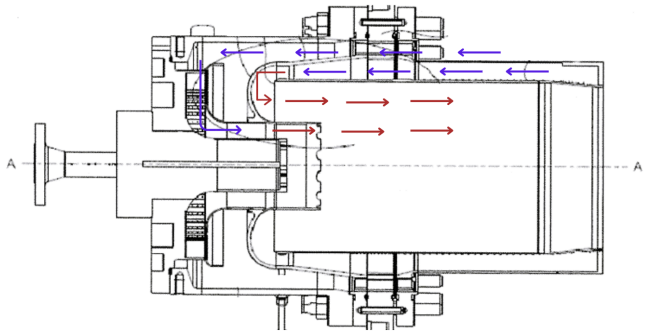

Figure 1.7: A schematic of FlameSheet™ burner [76]

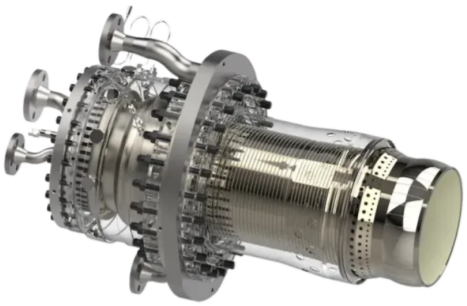

Figure 1.8: A rendered image of FlameSheet™ burner [26]

Further development of the FlameSheet™ burner is in progress within the Helios project, which is a cooperation between five partners (counting TU Delft) from three European countries [37].

1.3. Previous Work

The design of the actual FlameSheet™ burner is quite complex. A simplified geometry focusing on the key features was created that omits all auxiliary parts (Figure 1.9) for further study. Henceforth the FlameSheet™ burner will thus be referred to as a trapped vortex burner.

Gruber et al [35] conducted a comprehensive numerical investigation and an experimental study on the trapped vortex burner with hydrogen air mixtures at varying equivalence ratios to better understand flame stabilization and flashback phenomena in hydrogen air combustion. The experimental campaign, conducted at TU Delft, involved atmospheric pressure tests using a transparent combustor with optical access for diagnostics. Key measurements included velocity fields obtained through Particle Image Velocimetry (PIV) and flame visualization via Mie-scattering imaging. Figure 1.9 represents the schematic of the 2D FlameSheet burner and the diagnostic setup. The impact of different inner liner tips and channel height ratios was also investigated. The authors demonstrated that the flame stabilizes in a trapped vortex formed downstream of the 180° U-bend in the flow path (Figure 1.12) which leads to turbulent boundary layer disruption and higher flashback resistance [35] and that the flashback behavior depends strongly on the shape of the inner combustor-liner tip—either blunt or sharp as seen in Figure 1.10. Flashback takes place along an inner flame propagation route, around a blunt-shaped tip, or follows an outer flame propagation route along the burner dome wall, for a sharp-shaped tip.

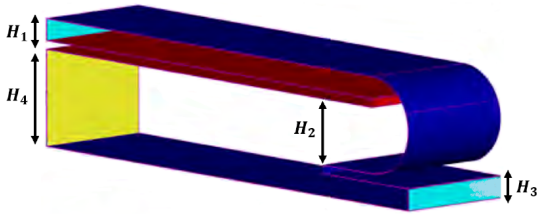

Figure 1.9: Schematic of the 2D FlameSheet burner and the diagnostic setup [35]

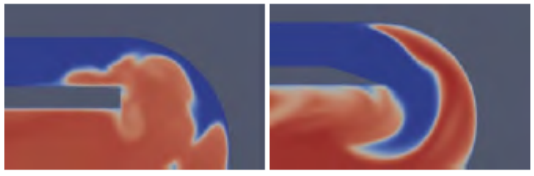

Figure 1.10: Instantaneous temperature field at the inception of flashback for the blunt and sharp tip [35]

The numerical simulations were carried out using OpenFOAM. The physical dimensions of the computational domain are scaled down to 1/2 of the dimensions of the combustor used in experiments. Large Eddy Simulations (LES) coupled with a Partially Stirred Reactor (PaSR) model were used to capture turbulent combustion dynamics with detailed hydrogen-air chemistry. The authors also reported a high-velocity region around the recirculation zone (Figure 1.11), which enhances the burner's flashback resistance by creating a barrier to the upstream flame propagation.

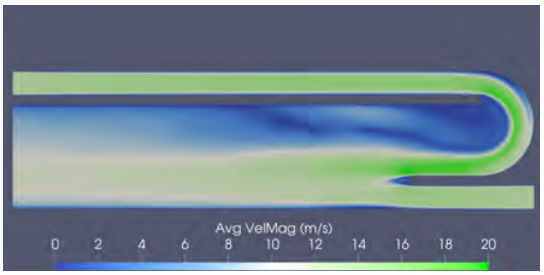

Figure 1.11: Average velocity field inside the burner [35]

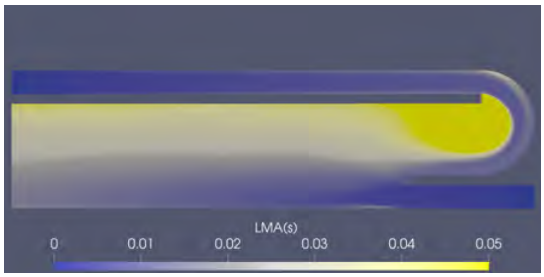

Figure 1.12: Local mean age (LMA) [35]

Hedge [36] performed a parametric study with Fluent [8], using RANS and LES to perform cold flow investigations and understand the effects of three geometric parameters on the flow dynamics 1.13:

1. Inner liner tip shapes (blunt (T1), semi-circular (T2), quarter-circular (T3), sharp flat (T4), sharp curved (T5)): From the results, for tips T2 and T3, the flow separates from the upper edge of the circular arc shaped tip and follows the shape of the outer bend before entering the downstream channel. Tips T4 and T5 also follow a similar pattern but we can clearly see a low velocity layer adjacent to the outer bend in the contour plots.
2. Channel height ratio (H2/H1): Reducing this ratio increased downstream velocity profile adjacent to the bend, a feature that could potentially improve flashback resistance.
3. Distance (D) between tip and outer bend wall: Smaller D reduced low velocity boundary layers near the outer wall.

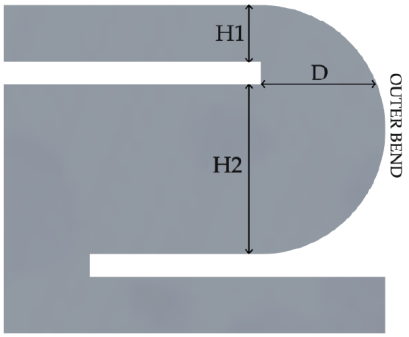

Figure 1.13: Burner geometry with dimensions H1, H2 and D shown [36]

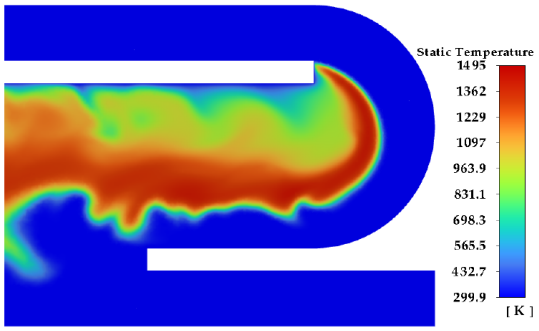

Figure 1.14: Temperature contour from reactive LES simulation [36]

Finally, reactive flow inside the burner was also simulated using the Artificially Thickened Flame Model (ATF) and the Li-Dryer mechanism [51] in Fluent to study the features of the H_2 flame. The same chemical mechanism was also used in the present study. An analysis which involved studying the temperature profile, shape of the flame front in the burner and also the diffusion of hydrogen into the flame was done. The temperature contour in Figure 1.14 shows the shape of the flame front. The stabilized flame in the U-bend has a smooth convex shape upstream, but downstream we see the presence of convex and concave shaped cusps.

The most recent (experimental) study was conducted by Zeman and Pichler [85], and focused on the flashback behavior of the trapped vortex burner with a sharp flat tip, for a range of equivalence ratios,

H_2 volume fractions and unburned mixture temperatures. The work also reports temperature profiles in the U-shaped bend region, with dependence on the Reynolds number and unburned inlet temperatures. The results from this work will help us increase the robustness of our numerical studies, in particular by providing us with more accurate temperature data for the inner liner tip. Figure 1.15 shows the measured Reynolds numbers at flashback. It depicts the ability of the trapped vortex burner to operate with very low equivalence ratios ($\phi <= 0.3$), which is the direct consequence of the recirculation zone generated by the novel geometry. Figure 1.16 reports the temperature profiles on the thin liner wall (shown in red in Fig. 1.9), moving away from the tip. Circular markers represent measurements in the middle of the liner (T_l), which we will be using in our work as boundary conditions.

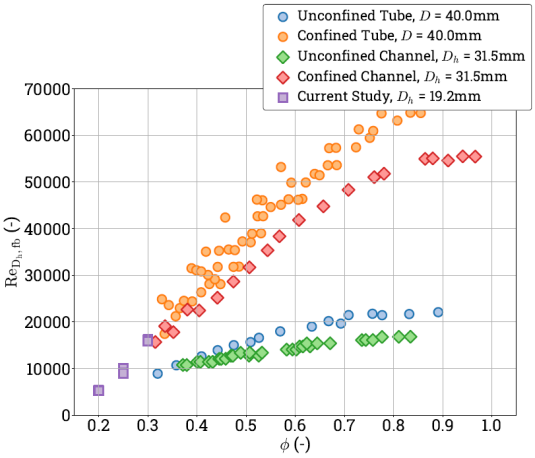

Figure 1.15: Reynolds number at flashback [85]

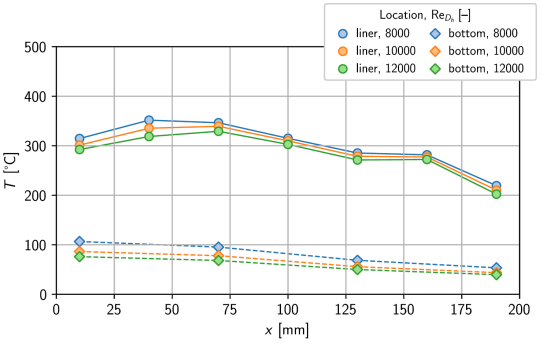

Figure 1.16: Steady-state streamwise temperature profiles in the middle (T_l) and at the bottom (T_{bp}) [85]

1.4. Research Objectives

The current work aims to accomplish the following objectives:

- What are the computational model requirements necessary to study the flame wall interactions in the trapped vortex burner?
  - It is necessary to have a computational model that can capture the flow inside the combustor. This involves determining appropriate mesh resolution especially near the walls. In addition, the selection of a suitable chemical kinetic mechanism for lean hydrogen–air combustion.
- How do different thermal boundary conditions on the liner walls affect flame stability, recirculation zone size and shape in lean premixed hydrogen combustion?
  - Wall thermal conditions are often oversimplified in simulations, yet they strongly influence near wall temperature gradients, heat loss, and local quenching. Simulations will be performed to examine the impact of three wall thermal treatments: 1) adiabatic, 2) isothermal (fixed at 300 K), and 3) spatially varying temperature profile derived from experimental measurements, by comparing flame shape, peak temperatures, recirculation zone size, and flame anchoring behavior under these conditions.
- Can a 2D simulation framework provide meaningful insights into flame wall interactions and flashback mechanisms compared to more expensive 3D simulations?
  - While 3D simulations capture full turbulent dynamics, they are computationally expensive. This study will evaluate the feasibility and limitations of using 2D simulations to study hydrogen-air combustion in a trapped vortex geometry.
  - The 2D results will be compared to prior 3D studies [36][35][25] to evaluate how well key flame flow features are reproduced.

1.5. Thesis Outline

This thesis report is divided into six chapters (including this one). In chapter 2, the fundamental principles of reactive turbulent flows are introduced, covering governing equations, chemical kinetics, and flame instabilities relevant to lean premixed hydrogen combustion. Chapter 3 details the numerical modeling approaches used in this work, including LES, combustion models, and the PeleLMeX solver. Chapter 4 describes the specific modeling approach adopted, including mechanism validation, mesh refinement, and boundary condition setup. Chapter 5 presents and discusses the results from cold and reactive flow simulations. Finally, Chapter 6 concludes the study and provides recommendations for future work.

2

Reactive Turbulent Flows

In this chapter, the theory behind combustion, turbulent flows and chemical kinetics of reactions will be discussed. Since this thesis investigates a turbulent hydrogen combustion setup, it is necessary to understand the basic principles and concepts which will be useful while performing and analyzing turbulent flow simulations.

Section 2.1 details the additional terms required to extend the Navier-Stokes equations for reactive flows and the significance of the equivalence ratio. Section 2.2 discussed the governing equations. Turbulent flows are addressed in Section 2.3, while Section 2.4 explains how reaction rates are computed, using chemical kinetics.

2.1. Introduction

Combustion involves multiple species reacting through multiple chemical reactions. A reacting gas mixture consists of multiple chemically active species whose behavior is governed by local thermodynamic conditions and reaction kinetics. The mixture may be isothermal or non-isothermal depending on the physical setup. The rates at which chemical reactions occur are influenced by factors such as temperature, pressure, and species concentrations. The key distinction between reactive and non-reactive flows lies in the role of species transport and chemical kinetics. While non-reactive flows can be described using classical fluid dynamics, reactive flows require a coupled treatment of fluid motion, species conservation, and reaction mechanisms, making their analysis more challenging and computationally intensive. For a cold flow, we solve for 5 variables but reacting flows require solving for N+5 variables, where N is the number of reacting species in the domain [64]. This requires more computational effort to compute the reacting flows as it increases the number of conservation equations required to solve.

The primitive variables for a three-dimensional compressible reacting flow are:

- The density $\rho = m/V$ [kg/m^3], where m is the mass [kg] and V is the volume [m^3];
- The velocity field $\mathbf{u} = (u, v, w)$ [m/s], with components u (x-direction), v (y-direction), and w (z-direction);
- One variable for energy e [J/kg], pressure P [Pa], enthalpy h [J/kg], or temperature T [K];
- The mass fractions Y_k, mole fractions (X_k) or concentrations (C_k) [$-$] of the N reacting species ($k = 1, \ldots, N$).

Species are characterized by their mass fractions Y_k for $k = 1$ to N where N is the number of species in the reacting mixture. The mass fractions Y_k are defined by:

$$Y_k = \frac{m_k}{m} \tag{2.1}$$

where m_k is the mass of species k present in a given volume V and m is the total mass of gas in this volume.

For a reactive mixture, the fuel and oxidizer mass fractions are important quantities; and their ratio is commonly used to characterize combustion properties [64]. Consider an overall unique reaction of type:

$$\nu'_F F + \nu'_O O \rightarrow Products \tag{2.2}$$

Here, ν'_F and ν'_O are the amount of moles of fuel and oxidizer, respectively. The mass fractions of fuel and oxidizer correspond to stoichiometric conditions when:

$$\left(\frac{Y_O}{Y_F}\right)_{\text{st}} = \frac{\nu'_O W_O}{\nu'_F W_F} = s \tag{2.3}$$

Where, W_O and W_F are molecular weights of oxidizer and fuel respectively and s is called the mass stoichiometric ratio [64]. Stoichiometry refers to the ideal chemical balance between fuel and oxidizer where all reactants are completely consumed, while the equivalence ratio quantifies how far a mixture deviates from this stoichiometric condition. The equivalence ratio of a given mixture is then:

$$\phi = s\frac{Y_F}{Y_O} = \left(\frac{Y_F}{Y_O}\right) / \left(\frac{Y_F}{Y_O}\right)_{\text{st}} \tag{2.4}$$

It can also be recast as [64]:

$$\phi = s\frac{\dot{m}_F}{\dot{m}_O} \tag{2.5}$$

where, $\dot{m}_F$ and $\dot{m}_O$ are respectively the mass flow rates of fuel and oxidizer. The equivalence ratio is a central parameter which helps characterize combustion regimes by indicating whether a mixture is fuel-lean, stoichiometric, or fuel-rich. It relates the flame characteristics, combustion efficiency, pollutant formation, and reaction kinetics, amongst others.

- $\phi < 1$ (Fuel-Lean Mixture): Excess oxygen is present, leading to efficient combustion but higher NO_x emissions.
- $\phi = 1$ (Stoichiometric Mixture): The exact amount of oxidizer is available to completely combust the fuel.
- $\phi > 1$ (Fuel-Rich Mixture): Excess fuel is present, leading to incomplete combustion and the formation of CO, unburned hydrocarbons, and soot.

2.2. Governing Equations

In this section, the various conservation equations (mass, species, momentum and energy), required to study reacting flows will be discussed [64].

2.2.1. Mass Conservation

The total mass conservation remains unchanged compared to non-reacting flows.

$$\frac{\partial \rho}{\partial t} + \frac{\partial \rho u_i}{\partial x_i} = 0 \tag{2.6}$$

where ρ is the fluid density [kg/m^3], which refers to only gas in this work, and u_i is the fluid velocity component [m/s].

2.2.2. Species Conservation

While the mass conservation equation ensures overall mass conservation, species conservation equations are required to track the evolution of individual chemical species involved in combustion. It accounts for species transport and chemical reactions. The mass conservation equation for species k is written:

$$\frac{\partial \rho Y_k}{\partial t} + \frac{\partial}{\partial x_i}(\rho u_i Y_k) = -\frac{\partial}{\partial x_i}(\rho V_{k,i} Y_k) + \dot{\omega}_k \tag{2.7}$$

for $k = 1, \ldots, N$, where $V_{k,i}$ is the i-th component of diffusion velocity [$\mathrm{m/s}$] of species k, and $\dot{\omega}_k$ is the reaction rate [$\mathrm{kg/(m^3 \cdot s)}$] of species k. The reaction rate will be discussed in detail in the following chapters.

Mass diffusion is a mass transport caused by gradients of temperature, pressure, concentration or electric potential [9]. On the right hand side of equation 2.7, the first term ($-\frac{\partial}{\partial x_i}(\rho V_{k,i} Y_k)$) represents a diffusive term which arises from Fickian diffusion [64].

Equation 2.8 represents the mass conservation constraint for diffusion velocities, ensuring that the sum of all species diffusion fluxes weighted by their mass fractions Y_k equals zero in any direction.

$$\sum_{k=1}^{N} Y_k V_{k,i} = 0 \tag{2.8}$$

In case of binary mixtures, the diffusion term $Y_k V_{k,i}$ can be approximated using the Fick's law which assumes the pressure gradients to be small, neglects volume forces and assumes the diffusion coefficients are the same [64]. This can be written as:

$$V_1 Y_1 = -D_{12} \nabla Y_1 \tag{2.9}$$

where D_{12} is the binary diffusion coefficient [$\mathrm{m^2/s}$].

For multicomponent systems it is not possible, in general, to derive relations for the diffusion fluxes containing the gradient of only one component. The Maxwell-Stefan equations will be used to obtain the diffusive mass flux. The Stefan–Maxwell equations provide a description of multicomponent diffusion without introducing explicit diffusion coefficients for every pair of species. From [56] we get the Stefan-Maxwell equation:

$$\sum_{\substack{j=1 \\ j \neq i}}^{N} \frac{X_i X_j}{\mathcal{D}_{ij}} \left(\vec{V}_j - \vec{V}_i \right) = \vec{d}_i - \frac{\nabla T}{T} \sum_{\substack{j=1 \\ j \neq i}}^{N} \frac{X_i X_j}{\mathcal{D}_{ij}} \left(\frac{D_{T,j}}{\rho_j} - \frac{D_{T,i}}{\rho_i} \right) \tag{2.10}$$

where X_i, X_j are the mole fractions, $\boldsymbol{V}_i$, $\boldsymbol{V}_j$ are the diffusion velocities, $\mathcal{D}_{ij}$ is the Maxwell diffusion coefficient, and $D_{T,i}$, $D_{T,j}$ are the thermal diffusion coefficients.

For an ideal gas the Maxwell diffusion coefficients ($\mathcal{D}_{ij}$) are equal to the binary diffusion coefficients (D_{ij}). If the external force is assumed to be the same on all species and that pressure diffusion is negligible, then $\vec{d}_i = \nabla X_i$. Since the diffusive mass flux vector is $\vec{J}_i = \rho_i \vec{V}_i$, where ρ_i is the partial density of species i defined as $\rho_i = \rho Y_i$. Then the above equation can be written as

$$\sum_{\substack{j=1 \\ j \neq i}}^{N} \frac{X_i X_j}{\mathcal{D}_{ij}} \left(\frac{\vec{J}_j}{\rho_i} - \frac{\vec{J}_i}{\rho_j} \right) = \nabla X_i - \frac{\nabla T}{T} \sum_{\substack{j=1 \\ j \neq i}}^{N} \frac{X_i X_j}{\mathcal{D}_{ij}} \left(\frac{D_{T,j}}{\rho_j} - \frac{D_{T,i}}{\rho_i} \right) \tag{2.11}$$

The linear system (equation 2.11) is obtained. Solving this system yields the diffusive fluxes $\vec{J}_i$ directly, which can be expressed as shown:

$$\vec{J_i} = -\sum_{j=1}^{N-1} \rho D_{ij} \nabla Y_j - D_{T,i} \frac{\nabla T}{T} \tag{2.12}$$

The first term on the right side represents Fickian diffusion term for multi-component mixtures which accounts for the fact that diffusion of species i depends not only on its own concentration gradient, but on all other species and the second term is the thermal diffusion term (Soret effect) which tells that even with no concentration gradient, temperature gradients can cause diffusion of species.

2.2.3. Momentum Conservation

Momentum conservation describes the balance of forces acting on a fluid element. The equation of momentum is the same for reacting and non-reacting flows [64]. For a Newtonian fluid, it is given by:

$$\frac{\partial}{\partial t}(\rho u_j) + \frac{\partial}{\partial x_i}(\rho u_i u_j) = -\frac{\partial P}{\partial x_j} + \frac{\partial \tau_{ij}}{\partial x_i} + S_{M,i} \tag{2.13}$$

where P is the pressure [Pa], $S_{M,i}$ is the volumetric source term or the body force and τ_{ij} is the viscous stress tensor [N/m^2] given by:

$$\tau_{ij} = -\frac{2}{3}\mu \frac{\partial u_k}{\partial x_k}\delta_{ij} + \mu\left(\frac{\partial u_i}{\partial x_j} + \frac{\partial u_j}{\partial x_i}\right) \tag{2.14}$$

where μ is the dynamic viscosity [Pa·s] and δ_{ij} is the Kronecker delta ($\delta_{ij} = 1$ if $i = j$ and 0 otherwise).

In the left-hand side of equation 2.13, the first term represents how the momentum changes with time and the second term describes how momentum is transported by the fluid's motion (convection). On the right-hand side, the first term represents the pressure gradient and the second term represents viscous forces, arising from internal friction within the fluid due to its viscosity, resisting deformation and smoothing out velocity gradients.

2.2.4. Conservation of Energy

Many forms of energy conservation equation exist in literature. Starting from the continuity equation, where the following equation holds for any quantity f:

$$\rho \frac{Df}{Dt} = \rho\left(\frac{\partial f}{\partial t} + u_i \frac{\partial f}{\partial x_i}\right) = \frac{\partial \rho f}{\partial t} + \frac{\partial \rho u_i f}{\partial x_i} \tag{2.15}$$

The conservation equation in terms of total energy e_t can be written as [64]:

$$\rho \frac{De_t}{Dt} = \frac{\partial \rho e_t}{\partial t} + \frac{\partial}{\partial x_i}(\rho u_i e_t) = -\frac{\partial q_i}{\partial x_i} + \frac{\partial}{\partial x_j}(\sigma_{ij} u_i) + \dot{Q} + \rho \sum_{k=1}^{N} Y_k f_{k,i}(u_i + V_{k,i}) \tag{2.16}$$

where $\sigma_{i,j}$ is the stress tensor [N/m^2].

Similarly the energy equation can be written in different forms in terms of energy and enthalpy including chemical terms and heat flux expression. For CFD codes sensible energies or enthalpies are sometimes preferred [64], which is written as:

$$\frac{\partial \rho h_s}{\partial t} + \frac{\partial}{\partial x_i}(\rho u_i h_s) = \frac{Dp}{Dt} - \frac{\partial q_i}{\partial x_i} + \tau_{ij}\frac{\partial u_i}{\partial x_j} + \dot{\omega}_T + \dot{Q} + S_H \tag{2.17}$$

where the third term on the right hand side is the viscous dissipation term, $\dot{Q}$ is the heat source term which is different from the heat released by combustion ($\dot{\omega}_T$) and the last term is the body force. The energy flux term (second term on the right side) includes a heat diffusion term from Fourier's law and a species diffusion related enthalpy term. The energy flux q_i is written as [64]:

$$q_i = -\lambda \frac{\partial T}{\partial x_i} + \rho \sum_{k=1}^{N} h_{s,k} Y_k V_{k,i} \tag{2.18}$$

Where λ is the thermal conductivity, with units of $\mathrm{W\,m^{-1}\,K^{-1}}$. The heat release $\dot{\omega}_T$ due to combustion is given by the equation below which links it to the species conservation equation 2.7:

$$\dot{\omega}_T = -\sum_{k=1}^{N} \Delta h^{\circ}_{f,k} \dot{\omega}_k \tag{2.19}$$

where $\Delta h^{\circ}_{f,k}$ is the standard enthalpy of formation [J/mol] of species k and $\dot{\omega}_k$ is the rate of production [mol/(m^3.s)] of species k.

2.3. Introduction to Turbulent Flows

Nearly all macroscopic flows encountered in real world and in engineering practice are turbulent. Turbulence in fluids is characterized by chaotic fluctuations in field variables like pressure, velocity and temperature over both space and time. These fluctuations occur over a wide range of time and length scales, creating eddies that transfer energy and momentum throughout the flow. Flows become unstable above a certain Reynolds number. As seen in figure 2.1, the boundary layer undergoes a distinct transition process: beginning as a laminar flow, it develops instability at the critical location(x_{cr}), then progresses through a transition region before becoming fully turbulent.

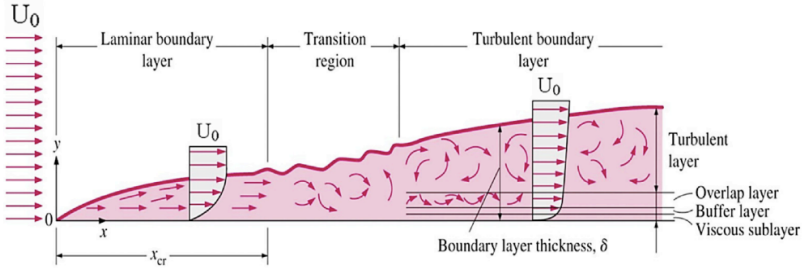

Figure 2.1: Laminar to turbulent transition[45]

Turbulent flows are accompanied by rotational flow structures called turbulent eddies with a wide range of length scales. The largest eddies which are highly anisotropic and most energetic interact and extract energy from mean flow by a process called vortex stretching while the smaller eddies are stretched strongly by larger eddies and weakly by the mean flow. Due to this the kinetic energy is handed down from larger eddies to progressively smaller and smaller eddies. This is called energy cascade[83].

The largest eddies are very sensitive to flow conditions and their sizes are close to the characteristic length of the flow($T \sim \frac{L}{U}$), similarly the smallest eddies are described by the Kolmogorov scales[83].

$$\eta = \left(\frac{\nu^3}{\varepsilon}\right)^{1/4}, \quad \tau_\eta = \left(\frac{\nu}{\varepsilon}\right)^{1/2}, \quad v_\eta = (\nu\varepsilon)^{1/4} \tag{2.20}$$

Here η is the Kolmogorov length scale (m), τ_η is the Kolmogorov time scale (s), and v_η is the Kolmogorov velocity scale (m/s). The variable ν represents the kinematic viscosity of the fluid (m^2/s), while ε denotes the turbulent kinetic energy dissipation rate (m^2/s^3).

Turbulent Boundary Layers

The concept of boundary layer was first proposed by Prandtl in the year 1904. He argued that fluid flow consists of two parts: flow closer to the surface (viscous part) and the flow away from the surface (inviscid part). In the thin boundary layer closer to the surface, viscous forces (effects of friction) are

dominant. Outside the boundary layer the flow is inviscid. The hypothesis of the adhesion of the fluid to the walls, or zero relative velocity between fluid and wall gave a very satisfying explanation for the process in the boundary layer[7].

In a turbulent boundary layer, the y+ value is a non-dimensional distance that is crucial for the modeling of turbulence, especially in computational fluid dynamics (CFD) simulations. The y+ value is defined as the distance from the wall to the first mesh node, based on local cell fluid velocity.

$$y^+ = \frac{yu_\tau}{\nu} \tag{2.21}$$

$$u^+ = \frac{u}{u_\tau} \tag{2.22}$$

Turbulent boundary layer can be divided into different regions depending on the Y+ values.

- **Viscous sub-layer ($y^+ < 5$)**:

  This region is dominated by viscous forces having negligible turbulence where velocity increases linearly with distance from the wall because of this the fluid layer adjacent to the wall is also known as linear sub-layer.

$$u^+ \approx y^+ \tag{2.23}$$

- **Buffer Layer ($5 < y^+ < 30$)**:

  This is a transitional zone between viscous and turbulent effects. Where both viscosity and turbulence play important roles. The velocity profile in this region is nonlinear.

- **Log-Law Region ($y^+ > 30$)**:

  Outside the viscous sub-layer a region exists where viscous and turbulent effects are important. The velocity profile in this region is given by:

$$u^+ = \frac{1}{\kappa}\ln(y^+) + B \tag{2.24}$$

  with $\kappa \approx 0.41$, $B \approx 5.0$.

  In figure 2.2 mean velocity profile of a smooth-flat-plate turbulent boundary layer plotted in log-linear coordinates with law-of-the-wall normalizations. For our work it is important to capture near wall effects. This will determine how accurately we capture flame flashback and its interaction with the boundary layer, particularly in regions where velocity gradients and turbulence levels significantly influence flame stabilization and propagation.

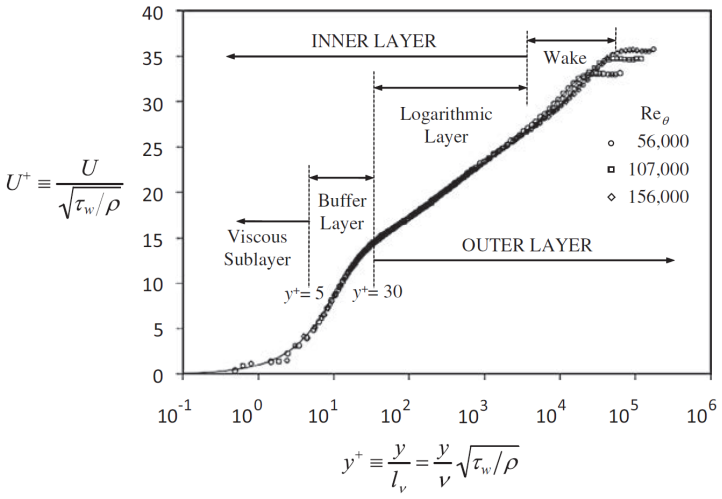

Figure 2.2: Mean-velocity profile of a smooth-flat-plate turbulent boundary layer plotted in log-linear coordinates with law-of-the-wall normalizations[46]

2.4. Chemical Kinetics

All chemical reactions take place at a definite rate, depending on the conditions of the system. In combustion modeling it is required to determine rates of reactant consumption and product formation. One particular species may be formed and consumed by in a number of different reactions, where some of these reactions may be reversible. Chemical kinetics deals with all of this.

2.4.1. Computation of Reaction Rates

The combustion process contains several chemical reaction. Consider a chemical system of N species reacting through M reactions, then a reaction can be represented by [64]:

$$\sum_{k=1}^{N} \nu'_{kj} M_k \rightleftharpoons \sum_{k=1}^{N} \nu''_{kj} M_k \quad \text{for} \quad j = 1, \ldots, M \tag{2.25}$$

where M_k is a symbol for species k, ν'_{kj} and ν''_{kj} are the molar stoichiometric coefficients of species k in reaction j. From mass conservation we can write:

$$\sum_{k=1}^{N} \nu'_{kj} W_k = \sum_{k=1}^{N} \nu''_{kj} W_k \quad \text{or} \quad \sum_{k=1}^{N} \nu_{kj} W_k = 0 \quad \text{for} \quad j = 1, \ldots, M \tag{2.26}$$

where

$$\nu_{kj} = \nu''_{kj} - \nu'_{kj} \tag{2.27}$$

For species k, the rate of production/consumption $\dot{\omega}_k$ is the sum of rates $\dot{\omega}_{kj}$ produced by all M reactions:

$$\dot{\omega}_k = \sum_{j=1}^{M} \dot{\omega}_{kj} = W_k \sum_{j=1}^{M} \nu_{kj} Q_j \tag{2.28}$$

where Q_j is the rate of progress of reaction j which can be expressed as[64]:

$$Q_j = K_{fj} \prod_{k=1}^{N} [X_k]^{\nu'_{kj}} - K_{rj} \prod_{k=1}^{N} [X_k]^{\nu''_{kj}} \tag{2.29}$$

where K_{fj} and K_{rj} are the forward and reverse rates of reaction j.

The forward rate constant K_{fj} for reaction j is independent of concentration and given by the Arrhenius expression which shows that the reaction rate increases exponentially with temperature, making it particularly relevant in high-temperature combustion reactions [64].

$$K_{fj} = A_{fj} T^{\beta_j} \exp\left(-\frac{E_j}{RT}\right) \tag{2.30}$$

where A_{fj} is the pre-exponential factor, β_j is the temperature exponent [dimensionless], E_j is the activation energy [J/mol], and R is universal gas constant (8.314 [J/mol·K]). T is the absolute temperature [K]. All of these constants are typically available in a "kinetic mechanism" file which will be discussed in the next section.

The backwards rates K_{rj} are computed from the forward rates through the equilibrium constants [64]:

$$K_{rj} = \frac{K_{fj}}{\left(\frac{p_a}{RT}\right)^{\sum_{k=1}^{N}(\nu''_{kj}-\nu'_{kj})} \exp\left(\frac{\Delta S_j^\circ}{R} - \frac{\Delta H_j^\circ}{RT}\right)} \tag{2.31}$$

where p_a is the atmospheric pressure [Pa], ΔH_j° is standard enthalpy change for reaction j [J/mol] and ΔS_j° is standard entropy change for reaction j [J/(mol·K)].

Properties such as heat capacity, enthalpy of formation, entropy, and Gibbs free energy play a crucial role in accurately modeling combustion processes. They are essential inputs for energy conservation, species transport, and reaction rate calculations. These values are typically provided along with the kinetic mechanism file (as discussed in the next section), as temperature fitted functions. The NASA polynomial coefficients formalism is adopted here.

2.4.2. Reaction Mechanisms

In chemical reactions, various intermediate species and transient bonds are formed. Elementary reactions are single-step processes that often involve reactive intermediates, including radicals. While some intermediates can be relatively stable, most radicals are highly reactive and short-lived [47]. Chemical kinetic mechanisms refer to the detailed sets of chemical reactions and associated rate parameters that describe how fuels and oxidizers interact, depending on temperature, to form products.

The computational cost of detailed mechanisms can be substantial and grows rapidly as the reaction mechanisms become more detailed. Therefore efforts have been made to develop more practical reaction schemes involving fewer reactions to represent combustion processes. These simplified schemes are called reduced mechanisms.

From Figure 2.3 we can see that kinetic mechanisms can generate similar or different results, depending on the kinetic values entered into them. Additionally, the dominant reactions within a mechanism can shift depending on the conditions, the specific reactions included in the mechanism file, and the techniques used to construct the mechanism, all of which influence the overall reaction rate and system behavior.

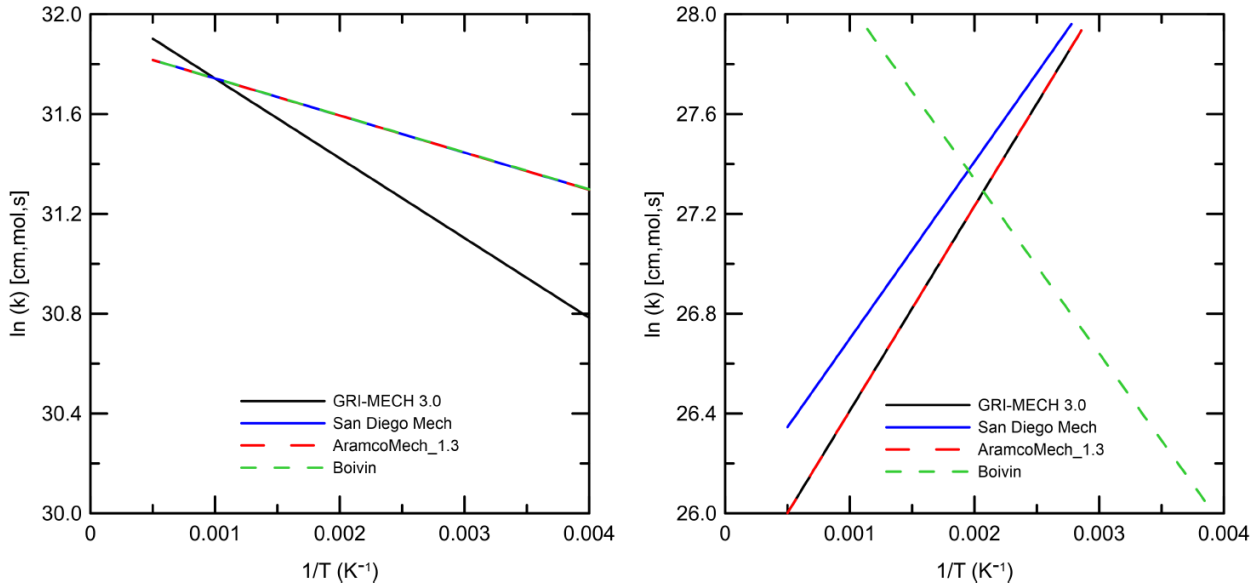

(a) $HO_2 + H \rightleftharpoons 2OH$ **(b)** $2HO_2 \rightleftharpoons H_2O_2 + O_2$

Figure 2.3: Representation of ln(k) vs 1/T using kinetic data for two H_2/O_2 combustion reations [31]

The slope of each line corresponds to the activation energy of the respective reaction mentioned in Figure 2.3. Differences in slopes between mechanisms indicate variations in predicted reaction rates for the same H_2/O_2 reactions. Diverging lines suggest discrepancies in rate constants due to different elementary reactions included in each mechanism and varying Arrhenius parameters for the same reactions. Before we choose a mechanism, we need to ensure that it will be valid for our problem of interest. For our hydrogen problem, we performed a validation step in simplified geometries under lean conditions against experimental data (see Section 4.1).

2.5. Premixed Combustion

Premixed combustion refers to a process where the fuel and oxidizer are homogeneously mixed before ignition. In such systems, the flame front propagates into the unburned premixed gases, and the local burning velocity determines the flame speed relative to the flow. This section explores the fundamentals of laminar and turbulent premixed flames. The laminar premixed flame represents a simplified model where the flame structure is smooth and steady while turbulent premixed flames are encountered in practical systems and are characterized by highly wrinkled and fluctuating flame fronts, significantly influenced by turbulent eddies interacting with the flame.

2.5.1. Laminar Flames

As shown in Figure 2.4, a one-dimensional, planar premixed flame can be divided into distinct regions. The propagation speed of a laminar flame relative to the mixture flow is called the laminar flame speed (S_L) which has units of [m/s]. The characteristic thickness of the flame is denoted by δ_L with units of [m]. From this schematic, we can identify four key regions in laminar premixed flames [49]:

- **Reactants zone**: This zone is located far upstream of the flame front, moving from left to right with velocity (u) equal to laminar flam speed (S_L) at a constant temperature (T_u). No reactions occur here.
- **Preheat zone**: Temperature of the unburnt mixture increases from T_u to ignition temperature T_{IG} by heat transfer from the reaction zone. This is a purely thermal diffusive region.
- **Reaction zone**: In this zone exothermic chemical reactions start dominating resulting in a rapid temperature rise and the species are converted from reactants to products rapidly due to high

reaction rates.

- **Products zone**: Burned gases at high temperature exist in this region.

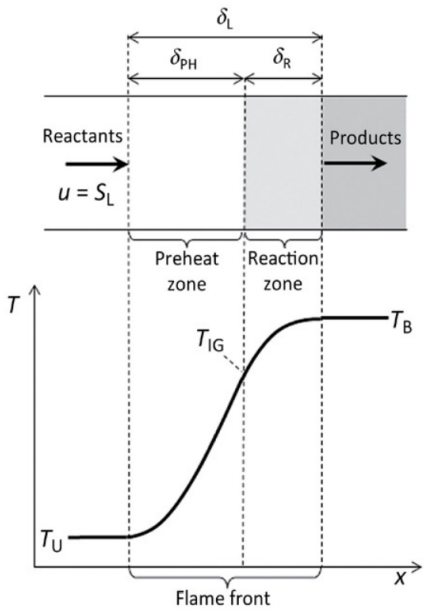

Figure 2.4: Schematic of a one-dimensional planar and unstretched flame front [12]

This one dimensional model highlights the fundamental thermo-chemical processes governing laminar flames. The interplay between heat transfer, species diffusion, and reaction kinetics in these zones and its predictable propagation characteristics are important to understand to further discuss turbulent flames in the next section as most combustion systems operate under turbulent conditions.

2.5.2. Turbulent Flames

Combustion, even without turbulence is a complex problem involving large range of chemical time and length scales. Turbulent combustion results from two way interaction of chemistry and turbulence. Turbulence alters the flame structure, which may enhance the chemical reactions but also, in extreme cases completely inhibit it, leading to flame quenching [64].

To classify turbulent flames into different regimes, as seen in Figure 2.5, three fundamental time scales need to be considered:

- **Turbulent/Integral time scale:** This scale (t_t) determines how long a turbulent eddy persists and influences the flame front before dissipating. It governs flame–turbulence interaction and flame wrinkling. It is defined as the ratio of the integral length scale to the velocity fluctuation of the largest eddy:

$$t_\mathrm{t} = \frac{l_0}{u'} \tag{2.32}$$

  where l_0 is the integral length scale $[\mathrm{m}]$, and u' is the root-mean-square velocity fluctuation $[\mathrm{m/s}]$, so t_t has units of $[\mathrm{s}]$.

- **Kolmogorov time scale:** This scale (t_k) characterizes the time it takes for the smallest turbulent eddies to complete a rotation or dissipate. It governs fine-scale mixing and molecular diffusion. It is defined as the ratio of the Kolmogorov length scale to the velocity fluctuation at that scale:

$$t_k = \frac{\eta_k}{u_\eta} \tag{2.33}$$

  where η_k is the Kolmogorov length scale $[\mathrm{m}]$, and u_η is the velocity fluctuation at the Kolmogorov scale $[\mathrm{m/s}]$, so t_k has units of $[\mathrm{s}]$.

- **Chemical time scale:** This scale (t_c) represents the characteristic time required for chemical reactions to convert reactants to products in the flame, or equivalently, the time it takes for the flame to propagate through its own thickness. It is defined as:

$$t_c = \frac{\delta_L}{S_L} \tag{2.34}$$

  where δ_L is the laminar flame thickness $[\mathrm{m}]$, and S_L is the laminar flame speed $[\mathrm{m/s}]$, so t_c has units of $[\mathrm{s}]$.

Based on these timescales, two dimensionless numbers are derived. The Damkohler number and Karlovitz number as well as the turbulent Reynolds number can be written as:

$$Da_T = \frac{t_t}{t_c} = \frac{l_0/u'}{\delta_L/S_L}, \qquad Ka_T = \frac{t_c}{t_k} = \left(\frac{\delta_L}{\eta_k}\right)^2, \qquad Re_T = \frac{u' l_0}{\nu} \tag{2.35}$$

Physically, these numbers provide insight into the interaction between turbulence and combustion:

- Damköhler number (Da_T) compares the turbulent time scale to the chemical time scale. A high Da_T indicates that chemical reactions are fast compared to turbulence, meaning the flame remains thin and well-defined (flamelet regime). A low Da_T suggests that turbulence dominates and can disrupt or broaden the flame front (distributed or broken reaction zones).
- Karlovitz number (Ka_T) compares the chemical time scale to the Kolmogorov (smallest eddy) time scale. It measures how deeply turbulence penetrates into the flame structure. Low Ka_T implies that only large eddies interact with the flame (wrinkled/corrugated flamelets), while high Ka_T means even the smallest eddies can disrupt the inner flame structure (thin reaction zones or beyond).
- Turbulent Reynolds number (Re_T) characterizes the intensity of turbulence by comparing inertial to viscous forces at the integral scale. Higher Re_T typically corresponds to a broader range of eddy sizes and more complex flame–turbulence interactions.

The regime diagram for premixed turbulent combustion, as shown in Figure 2.5, can be divided into different regions based on the relative the integral length scale (l_0) and the flame thickness (δ_L).

- **Laminar flames:** With $Re_T < 1$, the flames propagates smoothly with no turbulence effects. The flame maintains a perfectly laminar, undisturbed structure with no wrinkling or distortion
- **Wrinkled flames:** Moderate turbulence in this regime wrinkles the flame surface ($l_0 \gg \delta_L$) while maintaining $\eta_k > \delta_L$ ($Ka_T < 1$). This enhances the surface area which increases the burning rates.
- **Corrugated flames:** Stronger turbulence increases wrinkling compared to wrinkled flames while still preserving $\eta_k > \delta_L$. But the internal flame structure still remains laminar.
- **Thin reaction zone:** The kolmogorov eddies begin to penetrate the flame structure. The larger eddies still wrinkle the flame, while the smallest eddies disrupt the preheat zone. But the reaction zone itself remains thin and partially intact. This represents a transitional regime between flamelets and fully broken flames.
- **Broken reaction zone (Well-stirred reactor):** With very high turbulent intensities, the flame structure breaks down. Turbulent eddies penetrate both the preheat and reaction zones. The flame front disappears, and combustion occurs in isolated reaction zones that behave similarly to a well-stirred reactor.

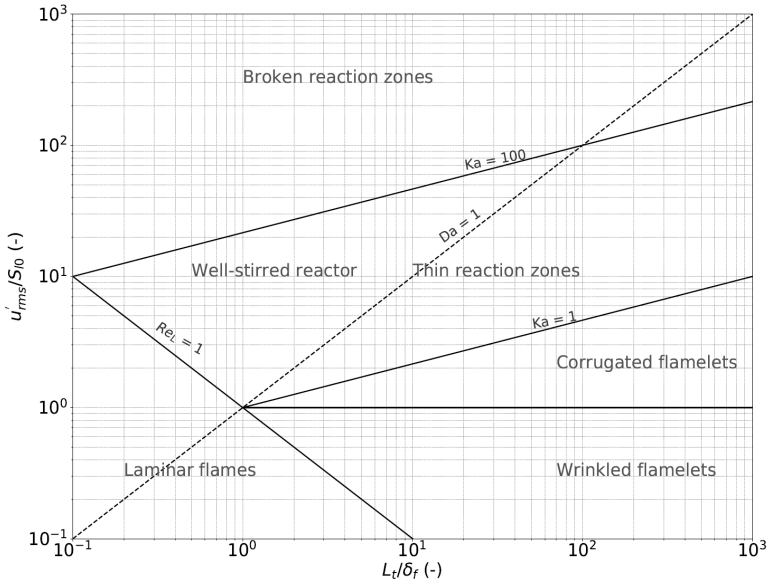

Figure 2.5: Regime diagram for premixed turbulent combustion[63]

2.6. Flame Front Instabilities

In premixed flames propagating at subsonic speed, intrinsic instability always appears due to interplay of several physical mechanisms. Hydrogen flames, in particular, exhibit strong instabilities. The two dominant mechanisms are thermo-diffusive instability and hydrodynamic instability also known as Darrieus-Landau Instability.

1. **Thermo-diffusive Instability:** Premixed H_2/air flames are characterized by sub-unity Lewis numbers and the strong influence of thermal-diffusive instability. If the molecular diffusion of reactants is higher than the thermal diffusivity (Le < 1), then the flame front is convex towards the fresh gases, as seen in figure 2.6: reactants diffuse towards burnt gases faster than heat diffuse towards cold fresh gases. These reactants are heated and then burn faster, increasing the local flame speed s_L. On the other hand, for fronts convex towards the burnt gases, reactants diffuse in a large zone and the flame velocity s_L is decreased [10]. This situation is unstable: the flame front wrinkling (as well as the flame surface) increases.

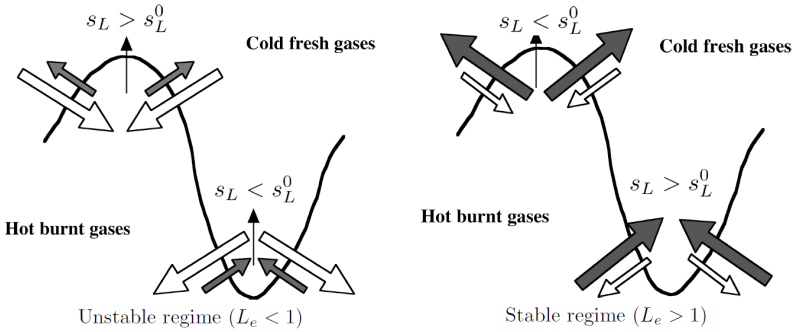

Figure 2.6: Thermo-diffusive instability. Grey arrow represents diffused heat and the white arrows represent diffused mass [64]

2. **Hydrodynamic Instability:** Hydrodynamic effects result from the omnipresent density jump across the flame leading to deflection of the streamlines ahead of a curved flame front [3]. Streamline divergence occurs upstream of convex towards the fresh mixture segments of the flame front, causing a decrease in the local flow velocity in comparison to the laminar flame speed. Upstream of concave segments streamlines converge, and the flow velocity is larger than the laminar flame

speed. This flow field variation, controlled by thermal expansion and viscosity, which further enhances the wrinkling of an initially weakly curved front as seen in Figure 2.7.

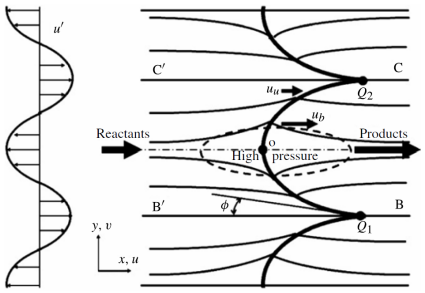

Figure 2.7: Schematic of the DL Hydrodynamic Instability [33]

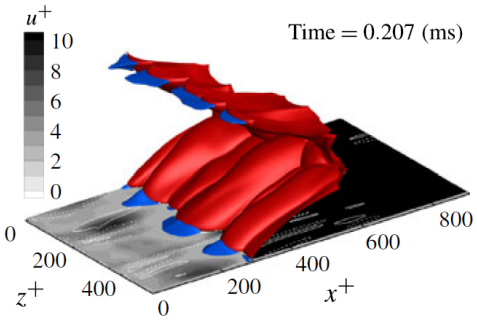

Figure 2.8: Non-dimensional streamwise velocity at y+=5 plane in a premixed flame [33]

From observations from [33], the physical mechanism of the backflow regions (blue surfaces in figure 2.8) is likely to be the origin of DL instability where the wrinkled flame surface affects the near-wall pressure field. This induces a positive pressure gradient immediately upstream of the flame bulge and causes flame flashback.

3

Numerical Modeling of Premixed Turbulent Flows

In this chapter, the numerical models employed to make the simulation of the reactive flow inside the trapped vortex hydrogen burner will be discussed. Section 3.1 introduces the different approaches to Computational Fluid Dynamics (CFD) investigations. Section 3.2 explains Reynolds decomposition and Favre averaging while Section 3.3 focuses on Large Eddy Simulation (LES). In Section 3.4 two classic subgrid scale models for turbulence are presented. In Section 3.5 different combustion models are discussed. Finally in section 3.6, the numerical solver PeleLMeX is explained. These sections will help in understanding the key differences between the various approaches and models.

3.1. Introduction

Hydrogen combustion has been extensively studied through experimental investigations, but with increasing computational power, CFD has become an essential tool for investigating combustion flows in complex geometries. Detailed numerical methods allow for realistic simulations which complement experimental data. In general, the approach for solving turbulent flow equations can roughly be divided into three classes [64] as seen in Figure 3.1:

- **Reynolds Averaged Navier Stokes (RANS)**: RANS equations are focused on solving the mean flow and the effects of turbulence on mean flow properties. The equations are obtained by ensemble averaging the instantaneous governing equations. The RANS equations require less computational resources for reasonably accurate results as compared to other two approaches.
- **Large Eddy Simulations (LES)**: This is an intermediate form of turbulent calculations where larger eddies are resolved while smaller ones are taken in consideration using sub-grid scale models. The small scale eddies are in general isotropic and have a universal behavior while the large scale eddies on the other hand are highly anisotropic and their behavior depends on the geometry of the domain and the boundary conditions. LES require finer grid cells compared to RANS but coarser compared to DNS.
- **Direct Numerical Simulations (DNS)**: These simulations solve full instantaneous Navier-Stokes equations without any model for subgrid scale quantities. The NS equations are solved on spatial grids that are sufficiently fine to resolve the Kolmogorov length scales.

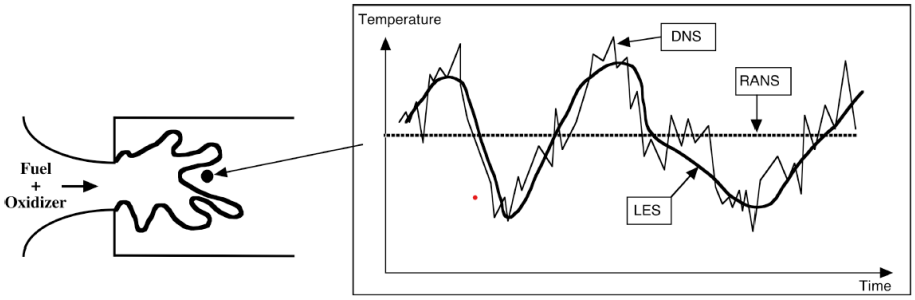

Figure 3.1: Time evolutions of local temperature computed with DNS, RANS or LES in a turbulent flame brush [64]

3.2. Reynolds Decomposition and Favre Averaging

RANS equations are extensively used in the industry for modeling turbulent flows. This is because they require least computational resources and time. This is done by decomposing the instantaneous components into a mean value with a fluctuating component superimposed on it as shown in Eq. 3.1.

$$f = \bar{f} + f' \quad \text{with} \quad \bar{f}' = 0 \tag{3.1}$$

For density-varying flows, any quantity f may be split into mean and fluctuating components using Favre averaging:

$$\tilde{f} = \frac{\overline{\rho f}}{\overline{\rho}} \tag{3.2}$$

Using this definition, f is decomposed as:

$$f = \tilde{f} + f'' \tag{3.3}$$

here, $\overline{\rho}$ denotes the Reynolds average of the density, while $\overline{\rho f}$ represents the Reynolds average of the product of the instantaneous density and the quantity f. The term $\tilde{f}$ is the Favre average of f. The quantity f'' denotes the Favre fluctuation component.

3.3. Large Eddy Simulations (LES)

Unlike RANS, which relies on ensemble averaging to model all turbulent scales, Large Eddy Simulation (LES) uses a spatial filtering operation to separate the large, energy-containing eddies from the smaller subgrid-scale (SGS) eddies. LES provides a better representation of unsteady, three-dimensional turbulent structures and is particularly well-suited for capturing the dynamics of turbulent reacting flows. In this work, we primarily rely on LES for simulating the combustion processes.

A filtered quantity $\overline{\phi}$ is defined as

$$\overline{\phi(x,t)} = \iiint G(x, x', \Delta)\phi(x', t)\, dx' \tag{3.4}$$

here, G is the LES filter function, and Δ is the filter cut-off length (for implicit LES) which is given by:

$$\Delta = (\Delta x \Delta y \Delta z)^{\frac{1}{3}} \tag{3.5}$$

The filtering operation are applied to the general equation mentioned in section 2.2 to give LES equations. The tilde operator represents Favre averaging[64].

- **Mass**:

$$\frac{\partial \overline{\rho}}{\partial t} + \frac{\partial}{\partial x_i}(\overline{\rho}\widetilde{u}_i) = 0 \tag{3.6}$$

- **Momentum**:

$$\frac{\partial \overline{\rho}\widetilde{u}_i}{\partial t} + \frac{\partial}{\partial x_j}(\overline{\rho}\widetilde{u}_i\widetilde{u}_j) + \frac{\partial \overline{p}}{\partial x_i} = \frac{\partial}{\partial x_j}\left[\overline{\tau_{ij}} - \overline{\rho}(\widetilde{u_i u_j} - \widetilde{u}_i\widetilde{u}_j)\right] \tag{3.7}$$

- **Chemical species**:

$$\frac{\partial(\overline{\rho}\widetilde{Y}_k)}{\partial t} + \frac{\partial}{\partial x_j}(\overline{\rho}\widetilde{u}_j\widetilde{Y}_k) = \frac{\partial}{\partial x_j}\left[\overline{V_{kj}Y_k} - \overline{\rho}(\widetilde{u_j Y_k} - \widetilde{u}_j\widetilde{Y}_k)\right] + \overline{\dot{\omega}}_k \tag{3.8}$$

- **Enthalpy**:

$$\frac{\partial \overline{\rho}\widetilde{h}_s}{\partial t} + \frac{\partial}{\partial x_j}(\overline{\rho}\widetilde{u}_j\widetilde{h}_s) = \frac{D\overline{p}}{Dt} + \frac{\partial}{\partial x_j}\left[\overline{\lambda\frac{\partial T}{\partial x_j}} - \overline{\rho}(\widetilde{u_j h_s} - \widetilde{u}_j\widetilde{h}_s)\right] + \overline{\tau_{ij}\frac{\partial u_j}{\partial x_i}} - \frac{\partial}{\partial x_j}\left(\rho\sum_{k=1}^{N} V_{kj}Y_k h_{s,k}\right) + \overline{\dot{\omega}}_T \tag{3.9}$$

All of the above equations contain unresolved fluxes due to the LES filtering operation. For momentum, these appear as Reynolds stresses:

$$\tau_{\text{sgs}} = \overline{\rho}(\widetilde{u_i u_j} - \widetilde{u}_i\widetilde{u}_j), \tag{3.10}$$

while in the chemical species and enthalpy equations, similar unresolved fluxes arise in the form of filtered scalar transport terms:

$$\overline{\rho}(\widetilde{u_j Y_k} - \widetilde{u}_j\widetilde{Y}_k), \quad \overline{\rho}(\widetilde{u_j h_s} - \widetilde{u}_j\widetilde{h}_s). \tag{3.11}$$

These sub-grid scale terms are modeled to account for the influence of unresolved small scale motions. Additionally, the chemical reaction source term, $\overline{\dot{\omega}}_k$, is filtered; see Section 3.5 for details on its treatment.

3.4. Turbulent Models

Since small scale eddies are approximately isotropic we can model them using eddy-viscosity approach:

$$\tau_{sgs} = -\nu_{sgs}\left(\frac{\partial \widetilde{u}_i}{\partial x_j} + \frac{\partial \widetilde{u}_j}{\partial x_i} - \frac{2}{3}\delta_{ij}\frac{\partial \widetilde{u}_k}{\partial x_k}\right) + \frac{1}{3}\tau_{kk}\delta_{ij} \tag{3.12}$$

here, ν_{sgs} is the sub-grid eddy viscosity and can be calculated using models like Smagorinsky model [72] and the wall-adapting local eddy viscosity (WALE) model [57], which are detailed briefly below.

3.4.1. Smagorinsky Model

It introduces an eddy viscosity based on the local strain rate of the resolved velocity field, assuming that subgrid stresses are aligned with the large-scale strain. The sub-grid eddy viscosity is given as [72]:

$$\nu_{\text{sgs}} = L_s^2(2\widetilde{S}_{ij}\widetilde{S}_{ij})^{1/2} \tag{3.13}$$

where, L_s is the Smagorinsky length scale, $\widetilde{S}_{ij}$ is the strain rate tensor. The Smagorinsky length scale is defined as:

$$L_s = C_s\Delta \tag{3.14}$$

The Smagorinsky model is the oldest LES model, but because of its simplicity it is widely used. But, it has some drawbacks like it tends to overpredict dissipation near walls due to dependence on strain rate alone, it requires wall-damping or dynamic modification near solid boundaries and the value of the constant C_s can depend on the flow conditions.

3.4.2. Wall-Adaptive Local Eddy (WALE)

An alternative to the Smagorinsky model is the Wall-Adaptive Local Eddy (WALE) viscosity model. It is an algebraic model which not only performs well close to the wall, but is also computationally less expensive. The subgrid eddy viscosity is calculated using the following relation [57]:

$$\nu_{\text{sgs}} = (C_w \Delta)^2 \frac{(S_{ij}^d S_{ij}^d)^{\frac{3}{2}}}{(\widetilde{S}_{ij}\widetilde{S}_{ij})^{\frac{5}{2}} + (S_{ij}^d S_{ij}^d)^{\frac{5}{4}}} \tag{3.15}$$

where, $C_w = 0.325$ is the WALE model constant, $\widetilde{S}_{ij}$ is the resolved strain rate tensor and S_{ij}^d is the traceless symmetric part of the velocity gradient tensor. The tensor S_{ij}^d is computed as:

$$S_{ij}^d = \frac{1}{2}(\widetilde{g_{ij}}^2 + \widetilde{g_{ji}}^2) - \frac{1}{3}\delta_{ij}\widetilde{g_{kk}}^2 \tag{3.16}$$

3.4.3. Sigma Model

Nicoud et al. [58] introduced the σ-model. The eddy-viscosity based, subgrid-scale model is derived from the analysis singular values of the resolved velocity gradient tensor. The model was introduced with the aim to overcome the limitation of classical models such as Smagorinsky and WALE by ensuring a set of desirable and numerical properties. The σ-model defines the subgrid-scale (SGS) viscosity as:

$$\nu_{\text{SGS}} = (C_\sigma \, \Delta)^2 \, D_\sigma, \tag{3.17}$$

where D_σ is a differential operator constructed from the singular values $\sigma_1 \geq \sigma_2 \geq \sigma_3 \geq 0$ of the velocity gradient tensor. These singular values are always real and non-negative, and they represent the local stretching and rotation characteristics of the resolved velocity field. This ensures the model contributes viscosity only when necessary.

$$D_\sigma = \frac{\sigma_3 \, (\sigma_1 - \sigma_2)(\sigma_2 - \sigma_3)}{\sigma_1^2}. \tag{3.18}$$

The constant $C_\sigma \approx 1.35$ is a model coefficient.

3.5. Combustion Models

In turbulent combustion modeling, the distinction between finite rate and infinite rate combustion approaches is fundamental to understanding the interaction between chemical kinetics and turbulent mixing. Early models such as Spalding's Eddy Break Up model [73] and the mixture fraction approach assumed infinitely fast chemistry, where chemical reactions occur instantaneously once the reactants are mixed. These infinite rate (or fast-chemistry) models allowed for relatively simple prediction of global flame features like flame length and mean temperature. However, such assumptions break down in conditions where the chemical timescales are comparable to or longer than the turbulent mixing timescales, as seen in lean flames [29]. These phenomena require finite rate combustion models, which explicitly account for the competition between turbulence and chemical kinetics. Finite rate models, including the flamelet [88], transported probability density function (PDF) [88] and Eddy Dissipation Concept (EDC) [55] approaches, provide a more accurate framework for predicting reaction zone structure, pollutant formation, and flame stabilization under conditions where the chemistry cannot be considered instantaneous.

Many practical combustion systems such as internal combustion engines and gas turbines operate within the wrinkled flame, corrugated flame, or thin reaction zone regimes. Consequently, much of the modeling focus has been on premixed turbulent combustion in these conditions. Each combustion model provides a closure for the mean or filtered reaction rates ($\overline{\dot{\omega}}_k$) as shown in Eq. 3.8, and therefore for the mean heat release rate, by making assumptions about how mixing, turbulence, and chemical kinetics interact. Combustion models are developed for specific regimes, as shown in Figure 2.5 based on non-dimensional number explain in section 2.5.2.

A variety of models have been developed to represent premixed turbulent combustion, each differing in how they capture the interaction between turbulence, mixing, and chemical kinetics. Among the more

recent developments, the Thickened Flame Model (TFM) [14] and the Flamelet Generated Manifold (FGM) [82] approach offer improved treatment of finite-rate chemistry and are particularly suited for high-fidelity CFD simulations. These models are discussed in detail in the following sections.

3.5.1. Flamelet Generated Manifold (FGM)

The Flamelet-Generated Manifold model shares the idea of flamelet approach [30], which proposes that under turbulent combustion, the chemical time scales are much shorter than the turbulent time scales such that a turbulent flame is an ensemble of laminar flames that have an internal structure not significantly altered by the turbulence. This approach assumes that the chemical composition and structure of the flame in multi-dimensional configurations closely follow the paths observed in 1D laminar flamelets.

FGM model precomputes a large set of flamelet solutions from detailed chemical kinetics and then storing them in a high-dimensional table, or manifold, indexed by a small number of control variables [82]. As a result of this, less controlling variables are sufficient to represent the combustion process. Therefore, the dimension of the look-up table can be kept low and during CFD, this table is accessed to reconstruct thermochemical states without solving full reaction kinetics directly. In the FGM framework, the chemical state of the flame is described by a small number of control variables, like a reaction progress variable Y_{cv} and, if required, the enthalpy h to account for heat losses. The progress variable Y_{cv} represents the advancement of the chemical reaction.

$$Y_{cv} = \sum_i c_i Y_i, \tag{3.19}$$

where the coefficients c_i are chosen such that $Y_{cv} = 0$ in the unburned mixture and $Y_{cv} = 1$ in the fully burned gas. During manifold generation, all species mass fractions and thermochemical quantities are expressed as functions of these control variables. Equation 3.9 can be reduced to a suitable form for laminar flamelet calculations used in the Flamelet-Generated Manifold (FGM) approach [82].

$$\frac{\partial \rho h}{\partial t} + \nabla \cdot (\rho \mathbf{v} h) - \nabla \cdot \left(\frac{\lambda}{c_p} \nabla h \right) = \nabla \cdot \mathbf{F}, \tag{3.20}$$

where $\mathbf{F}$ represents the enthalpy flux due to preferential diffusion:

$$\mathbf{F} = \sum_{i=1}^{N} h_i \left(\frac{1}{Le_i} - 1 \right) \frac{\lambda}{c_p} \nabla Y_i, \tag{3.21}$$

Due to the introduction of a manifold, all species mass fractions Y_i become functions of the controlling variables Y_{cv} and h. The manifold explained here corresponds to a non adiabatic premixed flamelet FGM. Therefore, the enthalpy flux can be expressed as:

$$\mathbf{F} = \sum_{i=1}^{N} h_i \left(\frac{1}{Le_i} - 1 \right) \frac{\lambda}{c_p} \left(\frac{\partial Y_i}{\partial Y_{cv}} \nabla Y_{cv} + \frac{\partial Y_i}{\partial h} \nabla h \right). \tag{3.22}$$

After some rearrangement and the introduction of a coefficient α, the enthalpy flux can be written as a function of the gradient of Y_{cv} only:

$$\mathbf{F} = \alpha \nabla Y_{cv}. \tag{3.23}$$

The coefficient α is stored in the FGM database together with the variables required to solve the conservation equations (i.e., ρ, λ, c_p, and ω_{cv}).

3.5.2. Thickened Flame Model(TFM)

The thickened flame model (TFM) also known as artificially thickened model (AFM) was first proposed by Butler and O'Rourke [14]. The approach models the flame front which is usually too thin to be resolved on a typical LES mesh, and simply perceived as a region of sharp discontinuity on a coarser

mesh by thickening the flame as seen in Figure 3.2 so the mesh can resolve the scalar gradients across the flame. This approach helps in capturing the flame dynamics and minimizing numerical diffusion errors due to a thin flame front.

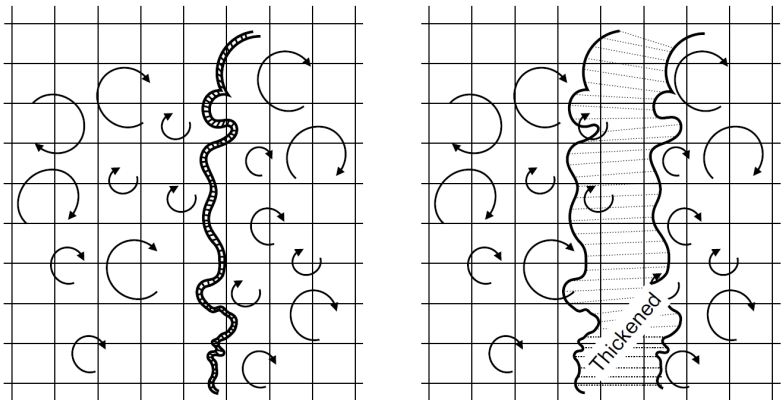

Figure 3.2: Artificially thickened flame, showing difference between actual and thickened flame [67]

The method is a spatial and temporal transformation of the flame from a coarse mesh to a finer mesh. The approach gives the same laminar flame speed (S_L) which is proportional to the square root of the thermal diffusivity (α) and the reaction rate ($\dot{\omega_k}$) by increasing the diffusivity and decreasing the reaction rate proportionally [67]:

$$S_L \propto \sqrt{\alpha \dot{\omega_k}} \tag{3.24}$$

The laminar flame thickness (δ_L) is inversely proportional to the laminar flame speed and can be expressed as:

$$\delta_L \propto \frac{\alpha}{S_L} = \sqrt{\frac{\alpha}{\omega_k}} \tag{3.25}$$

The thickening factor $\mathcal{F}$ is evaluated locally, based upon the values of a sensor Ω detecting the presence of a reaction front:

$$\mathcal{F} = 1 + (\mathcal{F}_{\max} - 1)\,\Omega \tag{3.26}$$

where $\mathcal{F}_{\max}$ depends on the local resolution Δx and is specified such that at least n points discretize the flame front:

$$\mathcal{F}_{\max} = \frac{n\,\Delta x}{\delta_l} \tag{3.27}$$

Here, n is the minimum number of points required to properly describe the flame front. All species diffusion coefficients, as well as the thermal conductivity, are multiplied by the thickening factor, and all reaction rates are divided by it. The sensor Ω is calculated as:

$$\Omega = \tanh\left(\beta \frac{\overline{|R|}}{\max(\overline{|R|})}\right) \tag{3.28}$$

where β is a constant and R is the reaction rate.

3.6. Numerical Solver - PeleLMeX

In this study, simulations are carried out using the Pele suite. Pele was developed as part of the US Department of Energy Exascale Computing Project (ECP) [66] for high-fidelity detailed simulations of turbulent combustion in open and confined domains. The Pele suite comprises PeleC, a compressible reacting flow block-structured adaptive mesh refinement solver and PeleLMeX, its low-Mach number counterpart. Both PeleC and PeleLMeX leverage the AMReX library [87], which allows Pele to implement a block structured AMR approach, an embedded boundary (discussed later in this section) formulation for complex geometries, and a performance portability framework for graphics processing unit (GPU) execution [27]. Both solvers share underlying software infrastructure, numerical methods, and parallelization strategies but there are differences, specifically with respect to the implementation of the low-Mach assumption. For this work we will be using PeleLMeX, applicable for the flow regimes under consideration. PeleLMeX uses a finite volume (FV) approach to solve the multi-species reacting Navier-Stokes equations in their low Mach number limit [18]. The Pele suite is publicly available at the software's GitHub repository [6].

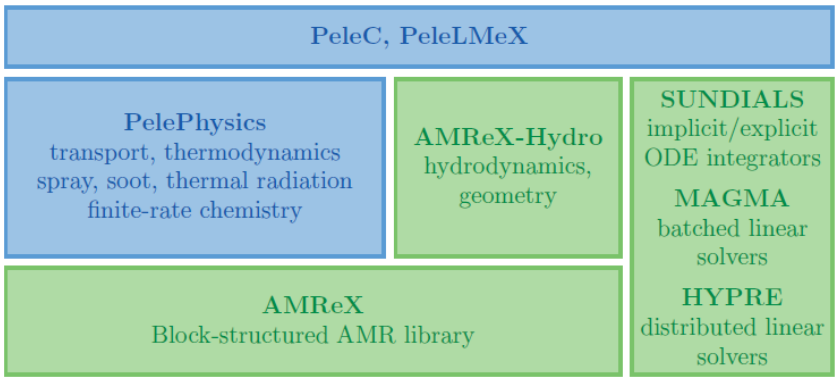

Figure 3.3: The Pele software suite (blue) and main libraries leveraged (green) [27]

PeleLMeX relies on several external libraries that provide essential capabilities for solving reacting-flow problems (Figure 3.3):

- PelePhysics handles the thermodynamic models and parameters, transport properties, chemical reactions and finite-rate chemistry integration (via SUNDIALS [28]).
- SUNDIALS (Suite of Nonlinear and Differential/Algebraic Equation Solvers) is an open-source library for solving stiff and non stiff ODE systems. Stiff ODE systems like reacting systems contain widely separated time scales, which generally require a very small time steps to remain stable, when explicit integration is considered.
- AMReX-Hydro which is a hydrodynamics library within the AMReX framework that implements the core numerical algorithms for advection.

In PeleLMeX, the advection components (larger time scales compared to diffusion) are treated explicitly with a 2nd order Godunov scheme modified for EBs, while diffusion is treated semi-implicitly with a Crank-Nicholson scheme. The stiff chemistry in the low-Mach limit is treated implicitly with CVODE which is a numerical solver offered through SUNDIALS. The overall time advancement scheme relies on a modified spectral deferred correction (SDC) algorithm [59]. The time step is constrained by the Courant–Friedrichs–Lewy (CFL) condition.

3.6.1. Finite Rate Chemistry

In reacting-flow simulations, the chemical source terms appearing in the species and energy transport equations represent the rates at which chemical reactions transform one set of species into another. When these reaction rates are computed explicitly from elementary chemical kinetics (see Eq. 2.29) based on the law of mass action and the Arrhenius rate law, the approach is termed finite-rate chemistry. In PeleLMeX, detailed finite-rate chemical kinetics are integrated without any subgrid combustion closure at this time (Section 3.5). Simulations are expected to use a mesh closer to DNS resolution,

where the need for a turbulent combustion model becomes less critical, since all fluctuations are resolved [29].

In each computational cell, the reaction source terms are evaluated directly from the local resolved thermodynamic fields. Using the Favre-filtered quantities defined in the LES formulation, the local reaction rate for species k is expressed as

$$\dot{\omega}_k^{\text{cell}} = \dot{\omega}_k(\widetilde{T}, \widetilde{Y}_i), \qquad \dot{q}_{\text{chem}}^{\text{cell}} = -\sum_k h_k(\widetilde{T})\, \dot{\omega}_k^{\text{cell}}.$$

where $\widetilde{T}$ and $\widetilde{Y}_i$ are the Favre filtered temperature and species mass fractions, respectively, and h_k is the specific enthalpy of species k. Here, $\dot{q}_{\text{chem}}^{\text{cell}}$ denotes the cell wise chemical heat release rate due to combustion. The filtered reaction rate $\overline{\dot{\omega}}_k$, which represents the LES filtered average of the instantaneous chemical source term, is approximated by evaluating the finite rate kinetics at the filtered variables:

$$\overline{\dot{\omega}}_k \approx \dot{\omega}_k(\widetilde{T}, \widetilde{Y}_i).$$

3.6.2. Embedded Boundary (EB) Approach

PeleLMeX uses EBs to represent geometrical objects within a structured grid without the need to body fitted mesh. In this approach the underlying computational mesh is uniform and block-structured, but the boundary of the irregular-shaped computational domain conceptually cuts through this mesh as seen in Figure 3.4. Each cell in the mesh becomes labeled as regular, cut or covered, and the finite-volume based discretization methods traditionally used in AMReX applications need to be modified to incorporate these cell shapes [77].

This relatively simple grid generation technique allows meshes for complex geometries to be generated quickly and robustly. But, the technique can produce arbitrarily small cut cells in the domain. AMReX provides the necessary EB data structures, including volume and area fractions. The fluxes, gradients and other numerical operators are adjusted to account only for the fluid region of the cells. The method might also involve generation of ghost cells or performing interpolation if a boundary condition is imposed directly on the embedded boundary surface.

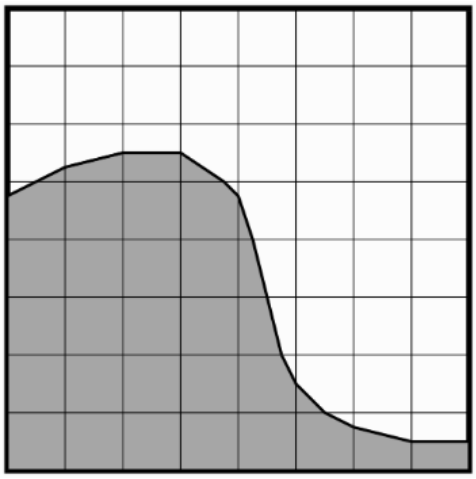

Figure 3.4: Rectangular mesh is cut by the irregular shape of the computational domain using EB approach [77]

4

Modelling Approach

This chapter includes the description of the numerical modeling approach used in PeleLMeX. Section 4.1 presents the selected chemical kinetics mechanism and its validation. Section 4.2 outlines the geometry description (using Pele's EBs) employed for cold and reactive flow simulations. In Section 4.3, a talk about different mesh refinement criteria used in PeleLMeX is followed by Section 4.4 which explains the selected boundary and initial conditions. Finally, in Section 4.5, a summary of the sampling strategy used for post processing is provided.

4.1. Mechanism Validation

The different kinetic mechanisms mentioned in Table 4.1, have different number of reactions and species involved. So, it is important to investigate their behavior against fundamental combustion properties like laminar burning velocity and ignition delay, in conditions similar to our problem of interest. These markers are experimentally measurable, making them ideal benchmarks to validate how well a chemical kinetic mechanism predicts real-world behavior. This is done with the help of an open source software Cantera [32]. The software is integrated as an extension package in a Python interface. For the laminar burning velocity computations, a FreeFlame object was used. This model solves the steady-state 1D premixed flame equations and allows for variable temperature, species, and velocity profiles across the flame. For the ignition delay calculations, an IdealGasReactor was used in Cantera. This reactor assumes constant volume, adiabatic conditions and a homogeneous mixture.

Table 4.1 shows five different mechanisms. Out of these five we chose to proceed with the LiDryer and Boivin mechanism for further analysis using Cantera. LiDryer and Boivin are well-established mechanisms widely used and validated in literature for (high-pressure) hydrogen combustion [86]. They have been tailored specifically for H_2/O_2 combustion. In contrast, mechanisms such as GRI-Mech 3.0, O'Connaire, and San Diego were developed primarily for hydrocarbon fuels and are less suitable for pure H_2 applications [62]. All mechanisms contain 9 species but they differ in their reaction networks, with the non-hydrogen-specific mechanisms introducing additional complexity and higher computational cost without corresponding benefits for H_2 focused simulations [62].

Mechanism	No. of species	No. of reactions	Reference
LiDryer	9	19	[51]
San Diego	9	21	[11]
O Conaire	9	19	[61]
Boivin	9	12	[13]
GRI Mech 3.0	9	24	[31]

Table 4.1: Mechanisms available for hydrogen combustion

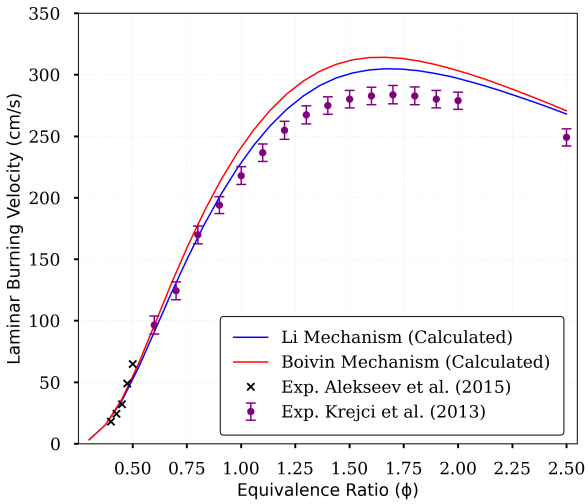

Figure 4.1: Laminar Burning Velocity vs Equivalence Ratio for H_2-air mixture at 1atm pressure and 298K unburned mixture temperature

Figure 4.1 compares laminar burning velocities from two kinetic mechanisms (Li and Boivin) with experimental data from Alekseev et al. [2] and Krejci et al. [44]. The equivalence ratio spans from lean to rich mixtures (0.50–2.50). The computational results show reasonable agreement with experiments, though deviations at ϕ <1.0 suggest potential refinements in the mechanisms' low-temperature kinetics. Peak velocities occur near stoichiometric conditions (ϕ=1.0), consistent with typical flame behavior.

Figures 4.2 and 4.3 present comparative ignition delay predictions using the Li and Boivin chemical kinetic mechanisms under varying conditions of pressure and equivalence ratio. In Figure 4.2, at ϕ = 1 and 2 atm, both mechanisms capture of ignition delay with increasing temperature (1000/T), with Li and Boivin curves nearly overlapping at higher temperatures and the Li mechanism giving slightly better results at low temperatures when compared with Konnov et al. [43]. Figure 4.3 compares how ignition delays at lean and atmospheric conditions (ϕ = 0.3, 1 atm) differ from the baseline case of ϕ = 1 at 2 atm. Since experimental data for such low equivalence ratio at atmospheric pressure was not available, this comparison highlights the relative behavior of the mechanisms. At leaner conditions and lower pressure, both mechanisms predict similar ignition delays.

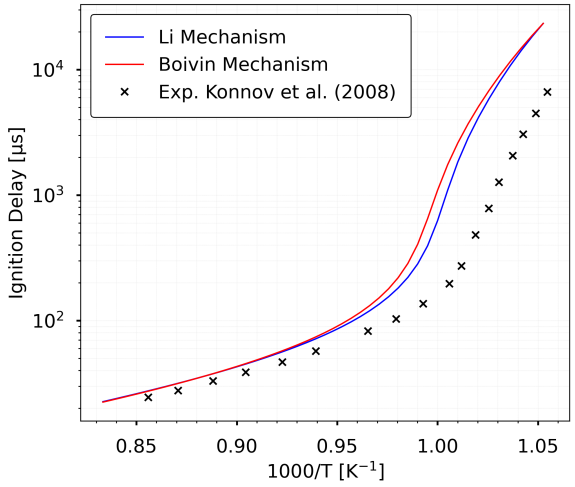

Figure 4.2: Ignition Delay Comparison for Li and Boivin Mechanisms at 2atm with $\phi = 1$

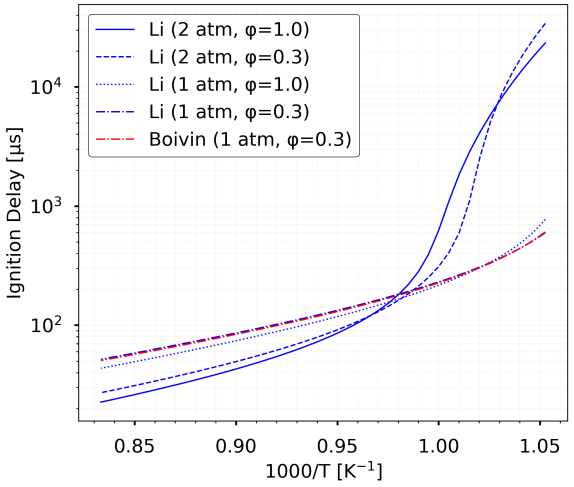

Figure 4.3: Ignition Delay Comparison for Li and Boivin Mechanisms at 1-2atm with $\phi = 0.3 - 1$

Among the two mechanisms evaluated, the Li mechanism shows better consistency with experimental laminar burning velocity data, while Boivin mechanisms slightly over predicts it. Also from Figure 4.2 the Li mechanism exhibits closer alignment with experimental ignition delay times at lower temperatures, while maintaining comparable performance to the Boivin mechanism at higher temperatures. These factors make the Li mechanism more reliable for hydrogen combustion modeling and justify its selection for our study. The reaction mechanism file for LiDryer mechanism is shown in Figure 4.4.

		A	n	E
H_2/O_2 chain reactions				
1. $H + O_2 = O + OH$		3.55×10^{15}	-0.41	16.6
2. $O + H_2 = H + OH$		5.08×10^{4}	2.67	6.29
3. $H_2 + OH = H_2O + H$		2.16×10^{8}	1.51	3.43
4. $O + H_2O = OH + OH$		2.97×10^{6}	2.02	13.4
H_2/O_2 dissociation/recombination reactions				
5. $H_2 + M = H + H + M^a$		4.58×10^{19}	-1.40	104.38
$H_2 + Ar = H + H + Ar$		5.84×10^{18}	-1.10	104.38
$H_2 + He = H + H + He$		5.84×10^{18}	-1.10	104.38
6. $O + O + M = O_2 + M^a$		6.16×10^{15}	-0.50	0.00
$O + O + Ar = O_2 + Ar$		1.89×10^{13}	0.00	-1.79
$O + O + He = O_2 + He$		1.89×10^{13}	0.00	-1.79
7. $O + H + M = OH + M^a$		4.71×10^{18}	-1.0	0.00
8. $H + OH + M = H_2O + M^b$		3.8×10^{22}	-2.00	0.00
Formation and consumption of HO_2				
9. $H + O_2 + M = HO_2 + M^c$	k_0	6.37×10^{20}	-1.72	0.52
$H + O_2 + M = HO_2 + M^d$	k_0	9.04×10^{19}	-1.50	0.49
	k_∞	1.48×10^{12}	0.60	0.00
10. $HO_2 + H = H_2 + O_2$		1.66×10^{13}	0.00	0.82
11. $HO_2 + H = OH + OH$		7.08×10^{13}	0.00	0.30
12. $HO_2 + O = OH + O_2$		3.25×10^{13}	0.00	0.00
13. $HO_2 + OH = H_2O + O_2$		2.89×10^{13}	0.00	-0.50
Formation and consumption of H_2O_2				
14. $HO_2 + HO_2 = H_2O_2 + O_2^e$		4.20×10^{14}	0.00	11.98
$HO_2 + HO_2 = H_2O_2 + O_2$		1.30×10^{11}	0.00	-1.63
15. $H_2O_2 + M = OH + OH + M^f$	k_0	1.20×10^{17}	0.00	45.5
	k_∞	2.95×10^{14}	0.00	48.4
16. $H_2O_2 + H = H_2O + OH$		2.41×10^{13}	0.00	3.97
17. $H_2O_2 + H = H_2 + HO_2$		4.82×10^{13}	0.00	7.95
18. $H_2O_2 + O = OH + HO_2$		9.55×10^{6}	2.00	3.97
19. $H_2O_2 + OH = H_2O + HO_2^e$		1.00×10^{12}	0.00	0.00
$H_2O_2 + OH = H_2O + HO_2$		5.8×10^{14}	0.00	9.56

Figure 4.4: The LiDryer mechanism for H_2/O_2 combustion [51]

4.2. Model Setup

The side view of the geometry used in this work is shown in Figure 4.5. This 2D version of the FlameSheet™ burner is more computationally affordable than its 3D counterpart. Gruber et al. [35] and Hegde [36] used a similar computational domain for their reactive and non reactive LES simulations, although they both had a non zero spanwise dimension (and the version from [35] had reduced dimensions). For our work we will be using the sharp liner tip.

PeleLMeX is developed in $C++$. In its current implementation the geometry is hard-coded within the source files rather than being read from external CAD files. The computational domain has been chosen to span 240 mm by 60 mm and the trapped vortex burner geometry has been created using the AMReX geometry classes. The embedded boundary module in AMReX represents geometries

as implicit functions (mathematical descriptions of shapes) which are then combined through boolean operations such as union, intersection, and difference to construct complex domains. The current implementation consists of six simple shapes, five of them can be seen in Figure 4.5 (white numbers) while the sixth was used for creating the sharp liner tip. After creating these individual components, the complete fluid region is obtained by taking the union of all components and then subtracting this combined shape from the outer, rectangular, computational domain.

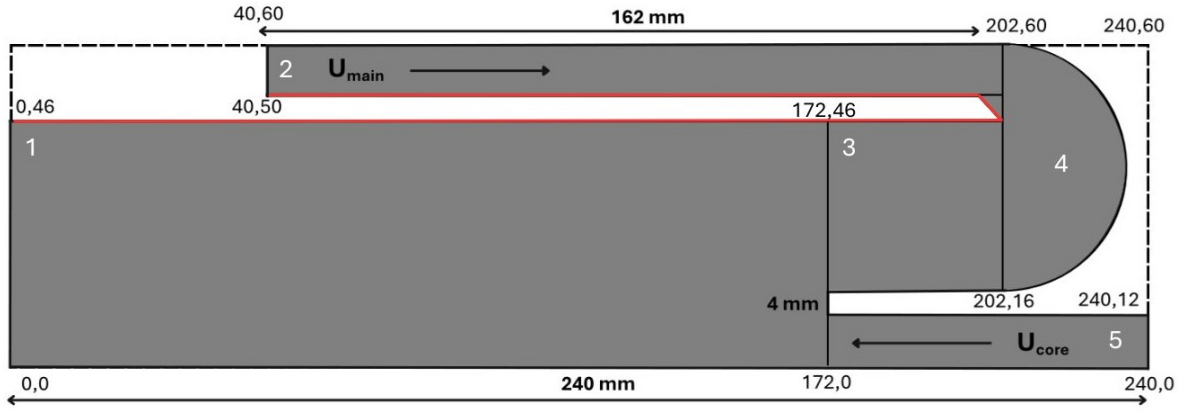

Figure 4.5: Side view of the trapped vortex burner with dimensions

4.3. Mesh Refinement

In this work, Adaptive Mesh Refinement (AMR) is heavily used. It enables to resolve regions of interest with higher spatial accuracy while keeping the computational cost manageable. The computational domain size, resolution, refinement levels and other parameters are set in the input source file.

The base mesh is defined with 256×64 cells at level 0, covering the full computational domain. We allow the solver to refine up to five additional AMR levels, with a refinement ratio of 2 in each direction between successive levels. This means that the smallest grid spacing is reduced by a factor of $2^5 = 32$ relative to the base grid. The refinement is updated every five time steps and includes two buffer cells around tagged cells. The blocking factor is set to 16 and the maximum grid size per AMR patch is limited to 32 cells in any direction.

In addition to AMR, localized fixed refinement regions are applied to ensure that the (y^+) remains below 1 near solid surfaces. A box-based refinement is used to increase resolution at both inlets, while EB-specific refinement is used to accurately capture the liner walls and curved geometrical features. The refinement parameters are configured to maintain sufficient grid resolution near critical flow regions and to resolve boundary-layer gradients effectively.

To have $y^+ < 1$ we require a sufficiently small first-layer cell height. Using the base (level 0) mesh we get a resolution of:

$$\Delta y_0 = \frac{0.06}{64} = 9.375 \times 10^{-4}$$

For a fully developed internal turbulent flow with $\mathrm{Re} = 1.2 \times 10^4$, the inlet velocity is $U = 10.2\ \mathrm{m/s}$, air density $\rho = 1.184\ \mathrm{kg/m^3}$, and kinematic viscosity $\nu = 1.561 \times 10^{-5}\ \mathrm{m^2/s}$.

Using the Blasius correlation for the Darcy friction factor (valid for $4 \times 10^3 \leq \mathrm{Re} \leq 10^5$):

$$f = 0.3164\,\mathrm{Re}^{-1/4} = 0.3164\,(12000)^{-1/4} \approx 0.0302,$$

giving a wall shear stress of

$$\tau_w = \frac{f}{8}\,\rho\,U^2 = \frac{0.0302}{8} \times 1.184 \times (10.2)^2 \approx 0.465\ \mathrm{Pa}.$$

The friction velocity is

$$u_\tau = \sqrt{\frac{\tau_w}{\rho}} = \sqrt{\frac{0.465}{1.184}} \approx 0.627 \text{ m/s}.$$

The first layer height corresponding to $y^+ = 1$ is

$$\frac{y^+ \nu}{u_\tau} = \frac{1.0 \times 1.561 \times 10^{-5}}{0.627} \approx 2.49 \times 10^{-5} \text{ m}.$$

Hence, the required first cell thickness is

$$y_1 \approx 2.5 \times 10^{-5} \text{ m}.$$

With a base mesh spacing of $\Delta y_0 = 9.375 \times 10^{-4}$ m and a refinement ratio of 2 per AMR level, the required number of AMR levels is L such that $\Delta y_L < y_1$:

$$\Delta y_L = \frac{\Delta y_0}{2^L} \quad \Rightarrow \quad 2^L \geq \frac{\Delta y_0}{y_1} = \frac{9.375 \times 10^{-4}}{2.49 \times 10^{-5}} \approx 37.7,$$
$$L \geq \log_2(37.7) \approx 5.23 \quad \Rightarrow \quad L_{\text{required}} = 6.$$

However, to be computationally manageable, the maximum allowed AMR levels is set to 5, giving a first-layer height of

$$\Delta y_5 = \frac{\Delta y_0}{2^5} = \frac{9.375 \times 10^{-4}}{32} \approx 2.93 \times 10^{-5} \text{ m},$$

corresponding to

$$y_5^+ = \frac{u_\tau \, \Delta y_5}{\nu} = \frac{0.627 \times 2.93 \times 10^{-5}}{1.561 \times 10^{-5}} \approx 1.18.$$

Thus, with 5 AMR levels, the near-wall resolution slightly exceeds $y^+ = 1$ but remains within the viscous sublayer.

4.4. Boundary and Initial Conditions

This section outlines the boundary and initial conditions used in the cold-flow and reactive-flow simulations, including the variations applied to the liner wall for the reactive-flow cases, which were introduced to assess the influence of thermal boundary effects on the overall flow and combustion behavior.

Table 4.2 summarizes the cold flow and reactive flow CFD cases investigated in this study.

Case	Dimension	Core Flow	Reynolds Number	Liner Walls BC
Cold Flow				
CF-1	2D	✓	12,000	No-slip, Isothermal (300 K)
CF-2	3D	✓	12,000	No-slip, Isothermal (300 K)
Reactive Flow				
RF-1	2D	✗	12,000	No-slip, Adiabatic
RF-2	2D	✗	12,000	No-slip, Isothermal (300 K)
RF-3	2D	✗	12,000	No-slip, Isothermal (F)
RF-4	2D	✗	8,000	No-slip, Adiabatic
RF-5	2D	✗	8,000	No-slip, Isothermal (300 K)
RF-6	2D	✗	8,000	No-slip, Isothermal (F)

Table 4.2: Summary of CFD cases simulated in this work. Symbols for the BC will be explained in Section 4.4.1. Case CF-2 was not simulated in the framework of this MSc thesis.

4.4.1. Boundary conditions

The computational domain contains four primary boundary types as seen in Figure 4.5. Both the main inlet and the core inlet are prescribed as velocity inlets, each with a bulk velocity of 10.2 m/s for the cold flow simulations (Re = 12000). For the reactive flow simulations, inlet velocities of 10.2 m/s and 6.8 m/s are examined, corresponding to Reynolds numbers of 12,000 and 8,000 respectively. In this case, the core inlet is sealed to maintain boundary conditions consistent with the experimental configuration.

The core inlet lies on the physical domain boundary, whereas the main inlet is defined on an embedded boundary (EB). The left boundary of the domain is specified as an outlet. All solid surfaces including the top and bottom channel walls as well as the burner liner are treated as no slip, adiabatic walls maintained at 300 K for the cold flow case, and the same wall conditions are applied in the reactive flow simulations.

The liner wall includes three segments colored in red, in Figure 4.5, and is assigned three different boundary conditions for tests and comparisons, in the reactive flow simulations. These conditions are: (i) a no slip isothermal wall maintained at 300 K, (ii) a no slip adiabatic wall, and (iii) a no slip isothermal wall with a spatially varying temperature profile (the F cases in Table 4.2). For the latter case, the wall temperature is prescribed using a third degree polynomial fit, based on measured liner temperature data from Zeman and Pichler [85]. The third degree polynomial was obtained by fitting the measured wall temperature data (converted to Kelvin) against their corresponding CFD coordinates (in meters). The polynomial coefficients were computed using a least squares regression (`numpy.polyfit`). The resulting function provides a smooth temperature profile suitable for numerical integration.

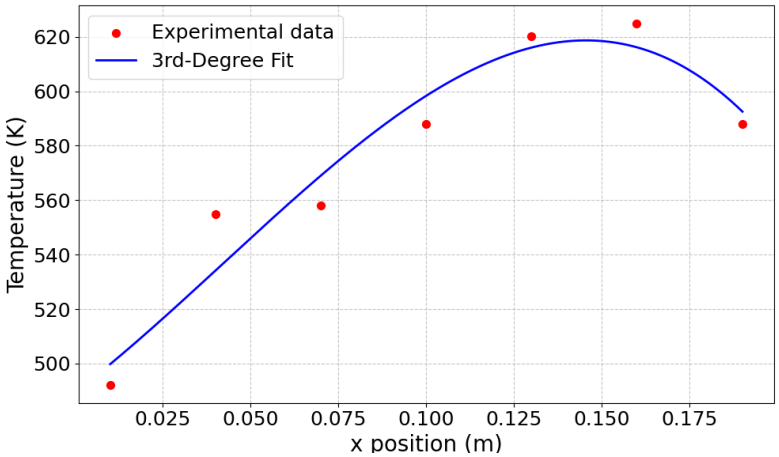

Figure 4.6: Third degree polynomial for temperature

The final polynomial for the temperature profile is given by

$$T(x) = -3.720 \times 10^4 x^3 + 4.722 \times 10^3 x^2 + 9.883 \times 10^2 x + 489.488 \tag{4.1}$$

4.4.2. Initialization of the Cold-Flow Simulations

The initial conditions in the simulation are set by computing the physical coordinates of each cell center based on the problem domain's lower bounds and the grid spacing. The flow is initialized with oxygen (O_2) and nitrogen (N_2) mass fractions of 0.233 and 0.767, respectively at 300 K (air composition). A uniform inlet velocity of -10 m/s is assigned in the x direction, while velocities in the other directions are set to zero in the entire domain. The solver starts by ensuring that the low-Mach condition is respected by recomputing the initial velocity field [60].

4.4.3. Initialization of the Reactive-Flow Simulations

The computational domain is initially filled with air (see above), with the temperature set to an initial value of 300 K everywhere. H_2 is introduced with a small mass fraction corresponding to $\phi = 0.2$ while O_2 and N_2 fractions are correspondingly adjusted to maintain overall mass balance, resulting in a locally premixed hydrogen air mixture in the inlet channel. Combustion is initialized with the help of a hot spot near the tip of the thin liner, consisting of a hot pocket of combusted mixture of H_2 and air, at $\phi = 0.2$ (computed via the use of Cantera), see Fig. 4.7. The velocity field is initialized with a uniform inflow of 10.0 m/s in the negative x direction, while the other velocity components are set to zero.

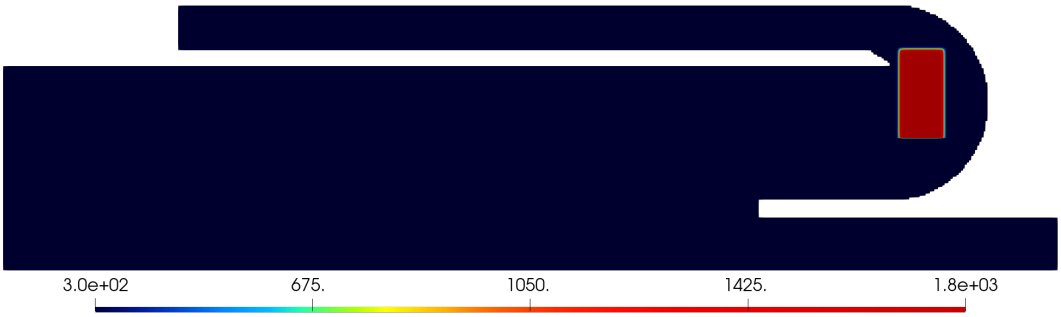

Figure 4.7: Temperature contour showing the combustion ignition hotspot

Using the equation of state, the density and enthalpy are calculated from the pressure, temperature, and species composition. Finally, species mass densities are initialized by multiplying the species mass fractions by the computed density, thus fully defining the initial thermochemical state of the flow field. Just as before, the solver starts by enforcing the low-Mach condition.

4.5. Sampling for Post Processing

The turbulent time scale represents the motion of large eddies in the turbulent flow. It gives an estimate of how quickly fluid properties change in time. It can be estimated in terms of flow properties, as:

$$\tau_0 = \frac{D_h}{U_u} = \frac{\rho_u D_h^2}{\mu_u Re_{D_h}}$$

Using,

$$\rho_u = 1.184\ \mathrm{kg/m^3}, \quad \mu_u = 1.846 \times 10^{-5}\ \mathrm{Pa \cdot s}, \quad D_h = 0.01\ \mathrm{m}, \quad Re_{D_h} = 12000,$$

$$\tau_0 = \frac{1.184 \times 10^{-4}}{0.22152} \approx 5.34 \times 10^{-4}\ \mathrm{s}.$$

where ρ_u, μ_u and U_u are the unburnt mixture density, dynamic viscosity and bulk velocity, respectively, and D_h is the inlet channel diameter. For exporting plot files from PeleLMeX, the acquisition time step

Δt_{pp} (time interval between consecutive output files) is chosen as a fraction of the turbulent time scale. Selecting Δt_{pp} as a small fraction of τ_0 guarantees that multiple acquisition time steps occur within one turbulent cycle, allowing accurate tracking of the temporal variations in flow quantities. This is necessary to properly account for transient turbulent structures and maintain convergence of statistical quantities.

$$\Delta t_{pp} = 0.3\,\tau_0 = 0.3 \times 5.34 \times 10^{-4} \approx 1.60 \times 10^{-4}\ \mathrm{s},$$

Finally, the total duration for data sampling is set to 30 times the turbulent time scale [71]:

$$t_{\mathrm{sample}} = 30\,\tau_0 = 30 \times 5.34 \times 10^{-4} \approx 0.0160\ \mathrm{s}.$$

5

Results and Discussion

This chapter will describe the cold and reactive flow simulations performed on the trapped vortex hydrogen burner. As per Table 4.2, 7 2D simulations were performed in this study, while the 3D blunt tip massively parallel simulation was already available from previous TUD work (which is important as it ensures that our choice of numerical options is adapted and can accurately capture flow features inside the burner). The simulations performed in this work are quasi-DNS (see explanation of Section 4.3). In DNS, all the length and time scales are completely resolved for both fluid motions and chemical reactions. Because of this a combustion DNS using detailed chemistry requires dozens of millions of CPU hours and generates hundreds of Terabytes of data [53], which is not practical for exploratory studies. It is a common practice, especially for turbulent reacting flows, to perform 2D investigations to evaluate models [5]. It provides a practical and scientifically valid alternative, especially when the goal is to probe sensitivity responses.

5.1. Cold Flow Simulations

5.1.1. 3D Cold Flow (Blunt Tip)

The two contour plots shown in Figure 5.1 represent velocity magnitude fields obtained from a 3D Large Eddy Simulation (LES) of the cold flow in the blunt tip burner geometry, at the mid plane of the domain. The LES uses the SIGMA model [58]. With LES we can observe transient features like turbulent structures throughout the shear layer and around the curved section of the burner, illustrating the inherently unsteady nature of the flow. We can see the flow separating from the outer wall of the curved region. The contour (b) represents a time averaged velocity magnitude plot. The averaging process smoothes instantaneous fluctuations. The mean field highlights the dominant flow patterns, including the high-velocity core and the low velocity or recirculation region. This averaged velocity distribution is used for comparison against experimental PIV measurements [4] and for validating the LES simulation.

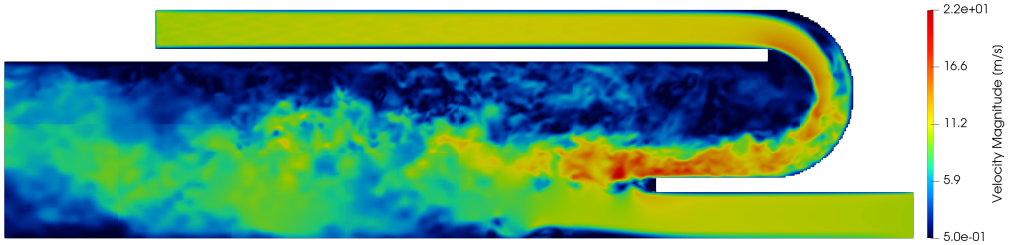

(a) Instantaneous velocity magnitude

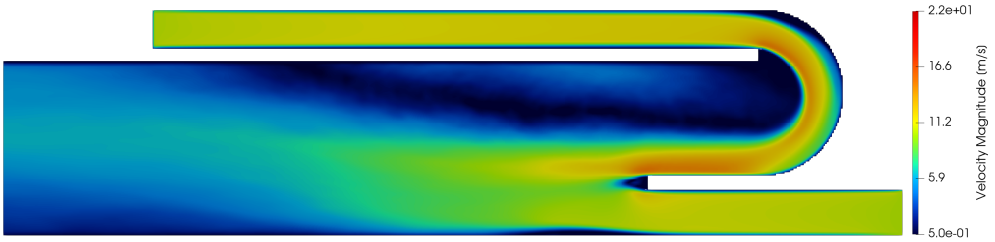

(b) Averaged velocity magnitude

Figure 5.1: Velocity magnitude contours from 3D LES

From the combustion Lab at TU Delft's Process and Energy Department, velocity data for seven profiles extracted at the location shown in Figure 5.2 are available [4]. These profiles are used to validate the cold flow LES simulation.

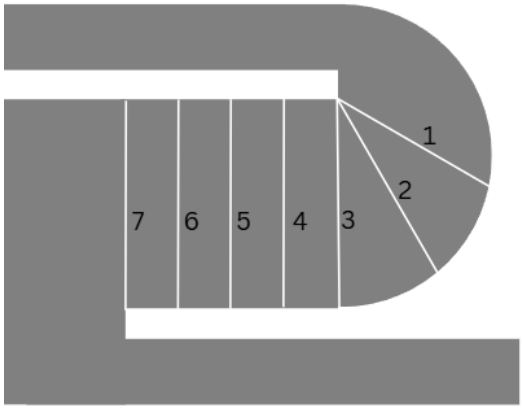

Figure 5.2: Profiles (1-7) along which normal velocities are obtained using PIV

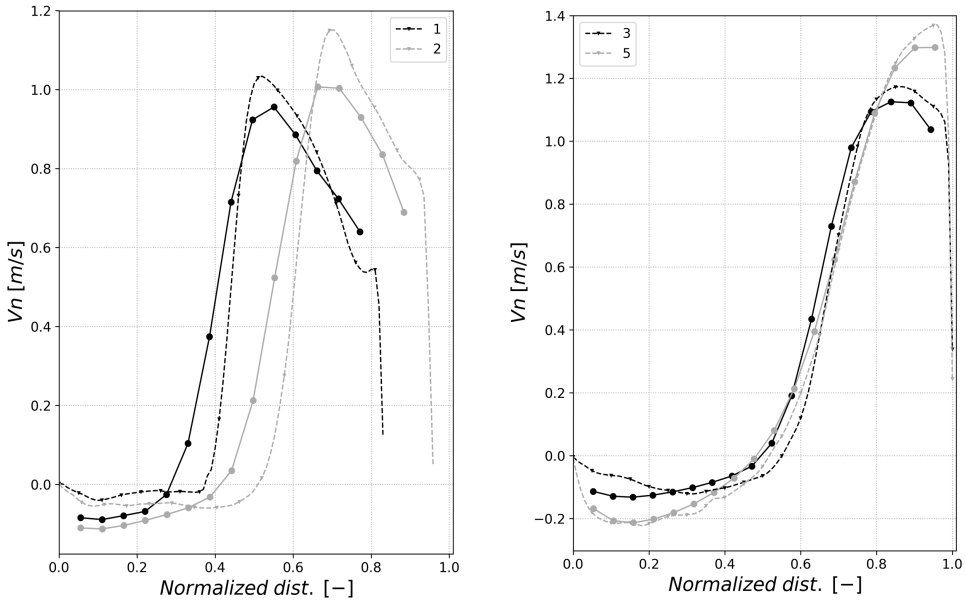

(a) Along curves 1 and 2

(b) Along curves 3 and 5

Figure 5.3: Comparison of normal velocity profiles from LES with PIV data

Comparisons results for 4 locations are shown in Figure 5.3. In these plots, the normal velocity at the curves' location are non dimensionalized using the bulk velocity (10.2 m/s). All the profiles show a slightly higher peak velocity than the PIV data. The shear layer is also more stable in the LES, which is consistent with not using an inlet turbulent profile. Overall, the LES simulations show a good agreement with the PIV velocity profiles and enable to validate the computational approach.

Figure 5.4 shows a 3D visualization of the turbulent structures via the Q criterion. Note that this simulation was performed with the blunt tip burner configuration. These structures are particularly dominant downstream of the bend, where strong shear layers and flow curvature lead to enhanced turbulence production. The visualization helps show how vortices form, break down, and move through the burner, giving a clear picture of how turbulence develops and how it affects the mixing of the flow.

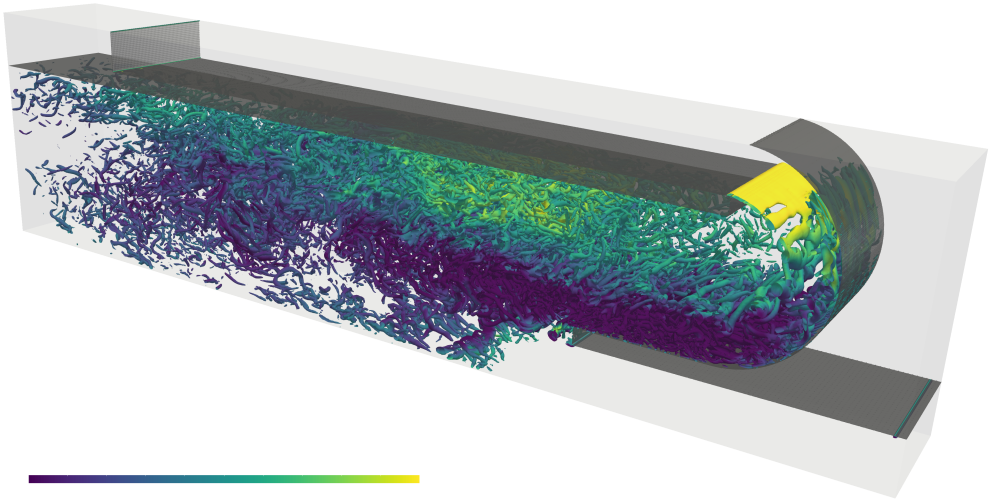

Figure 5.4: Q-Criterion Visualization

5.1.2. 2D Cold Flow (Sharp Tip)

Figure 5.5 and 5.6 shows the instantaneous and time averaged velocity magnitude contours for the cold flow simulation with a sharp tip. Figure 5.5, illustrates the turbulent behavior of the flow while Figure 5.6 displays the resulting mean velocity distribution. A 2D simulation cannot capture the full spectrum of turbulent motions or out of plane vortices, resulting in a less realistic representation of turbulence compared to a 3D simulation. Also, the change in tip geometry produces noticeable differences in the flow development. In the sharp tip geometry the incoming jet follows the shape of the sharp tip with a clear acceleration of the flow around the leading tip and we see a low velocity layer adjacent to the outer bend. These flow patterns are consistent with the 3D sharp tip simulations performed by Hedge [36]. However, the instantaneous plot also shows larger and more frequent release of small scale vortices near the tip which was not seen in the previous study [36].

The averaged velocity field is smoother, but the influence of the sharp tip remains visible. Figure 5.6 compares the average velocity magnitude contour of our work with Hegde. A comparison of the flow fields indicates that the core jet adheres to the sharp tip similarly in both 2D and 3D simulations. However, the 3D result exhibits some difference, after the U bend the trajectory of the high velocity jet gets close to the liner walls in the recirculation region which could influence the trapped vortex. Because 2D simulation lacks the 3D turbulent cascade responsible for transferring energy to smaller scales, the effective turbulence dissipation is lower. As a result, 2D simulation exhibits unrealistically high velocities relative to its 3D counterpart.

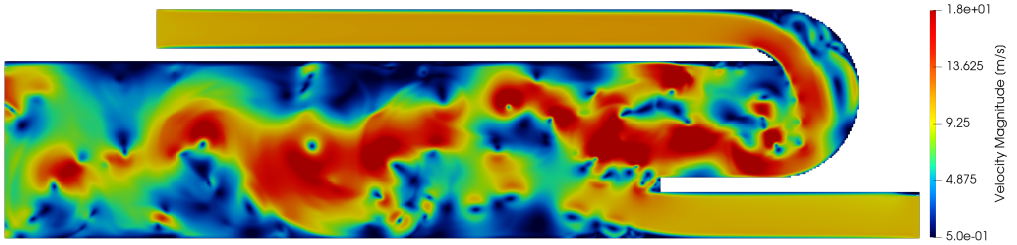

Figure 5.5: Instantaneous velocity magnitude

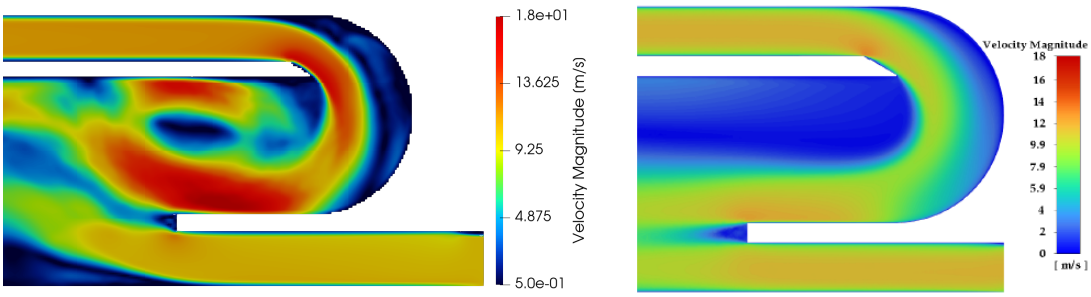

(a) Averaged velocity magnitude 2D

(b) Averaged velocity magnitude 3D [36]

Figure 5.6: Comparison of average velocity magnitude with Hegde

5.2. Reactive Flow Simulations

5.2.1. Instantaneous flame analysis

Figure 5.7 shows instantaneous temperature contours of the six reactive cases that were simulated in this work with varying thermal BC for the liner walls and main flow Reynolds number. The first column corresponds to results for Re = 12,000 while the second column shows results for Re = 8,000. Cases in first, second and third row have adiabatic, isothermal (300K), and temperature fitted isothermal boundary condition, respectively, with the core flow inlet Reynolds numbers Re_{core} = 0 (plugged core flow inlet).

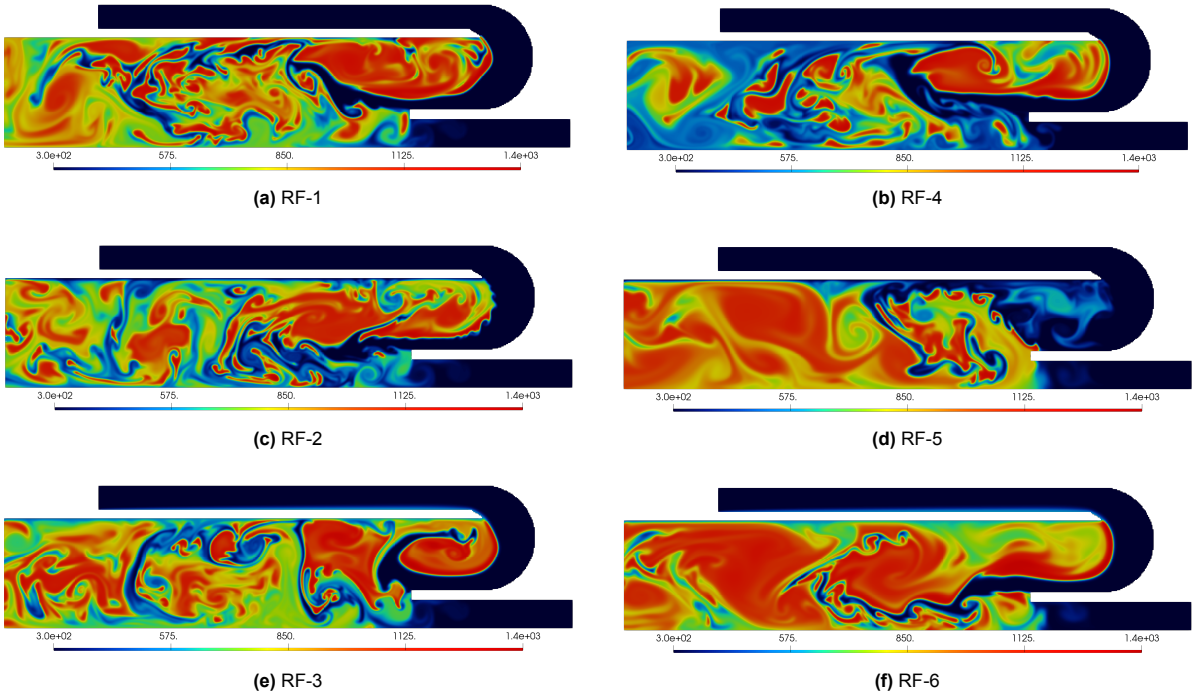

(a) RF-1 **(b)** RF-4

(c) RF-2 **(d)** RF-5

(e) RF-3 **(f)** RF-6

Figure 5.7: Instantaneous temperature contours from 2D DNS

At the higher Reynolds number, the flow is more turbulent, and the adiabatic boundary condition in case (a) produces a hotter flame. Since no heat is removed at the liner walls, the gas adjacent to the wall remains hot, resulting in a very stable flame strongly anchored at the sharp tip. The flame front gets disturbed by vortices/turbulent structures but remains anchored at the tip. The recirculation region enhances mixing, supporting continuous combustion and preventing local extinction. As a results RF 1 produces a stable flame. For RF-2 (c), with the 300 K isothermal liner walls, the cold boundary extracts heat from the flame, acting as a strong heat sink. At $\mathrm{Re} = 12{,}000$, the enhanced turbulent mixing pushes hot products into contact with the cold wall more frequently, causing periodic quenching of the flame tail. As a result the flame gets extinguished. A similar extinction behavior was also reported by Gruber et al. [35]. For RF-3 (e), the fitted temperature boundary condition introduces a spatially varying wall temperature, but the overall turbulent flow dynamics remain similar to the adiabatic case. However, unlike the adiabatic wall, the incoming mixture through the main inlet along the wall is slightly preheated. At the sharp tip the flame gets partially quenched as it tries to anchor. The flame front gets periodically disturbed by the turbulent structures, particularly the cold flow being recirculated and mixing with the burnt gases, but the flame is able to reattach itself. Even though unsteady vortices persist in destabilizing the flame, the system seems to be able to maintain combustion and avoid full extinction.

At $\mathrm{Re} = 8000$, the flame exhibits significantly lower turbulence intensity, which enables transition towards a quasi laminar regime. Under adiabatic conditions (b), the flame front remains mostly undisturbed, and anchored at the tip and the inner liner wall. In case (d) for the isothermal wall at 300 K, the behavior is similar, although the limited ability of the flow to transport heat back into the flame along

with a high heat loss through the wall results in the flame getting detached from the wall and leaving the domain in an nonphysical way, going through a brief period of anchoring near the lowest liner, as seen in figure 5.7 (d). Finally, in case RF-6 (f) the fitted temperature at $\mathrm{Re} = 8000$, the spatially varying liner temperature produces a flame wall interaction that is much more physical. The lower turbulence intensity at this Reynolds number results in reduced turbulence, allowing the imposed wall temperature profile to influence the flame more directly. As a result, the flame remains more laminar, more stable, and more often anchored than at $\mathrm{Re} = 12{,}000$. Because 2D simulations capture low-Reynolds-number behaviour more reliably than highly turbulent flows, and because the fitted temperature BC is derived from experimental measurements, this case provides the most realistic representation of the flame structure amongst all 2D cases considered. Based on the observations discussed above, cases (c) and (d) will not be considered for further analysis. In both configurations, the flame is unable to sustain itself. Further examination of these extinguished cases would not provide additional physical insight.

5.2.2. Averaged fields

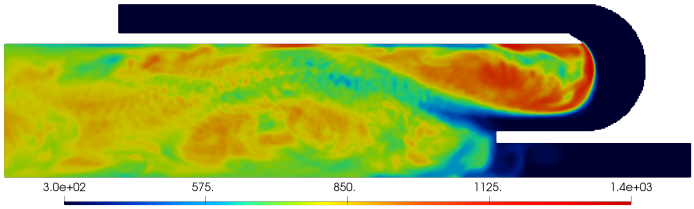

(a) RF-1

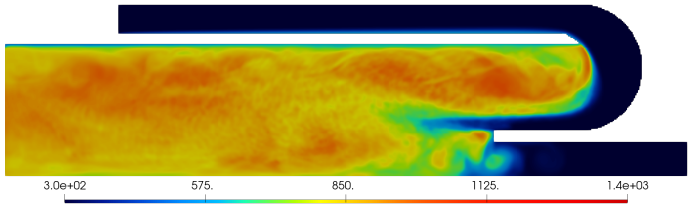

(b) RF-3

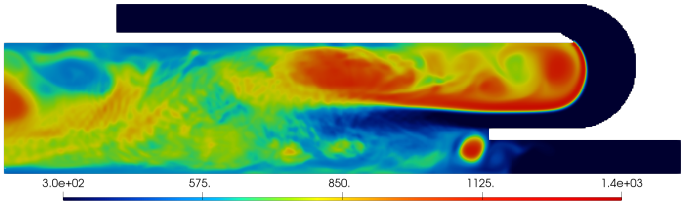

(c) RF-4

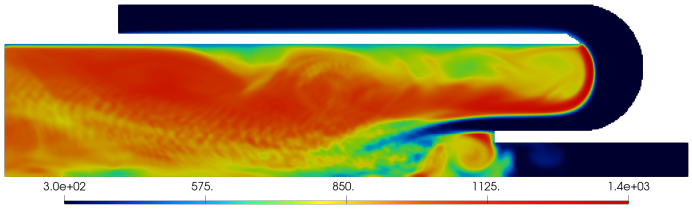

(d) RF-6

Figure 5.8: Averaged temperature contours from 2D DNS

Figure 5.8, shows the averaged temperature contours for the four reactive cases which maintained a stable flame. While the instantaneous fields reveal the highly unsteady behavior of the flame and the surrounding flow, the time averaged fields filter out these fluctuations and expose the underlying mean flow structure. The averaged contours highlight features like as the recirculation zone, the flame

position, and the long term influence of thermal boundary conditions. These mean quantities provide a clearer and more reliable representation of the global flow behavior. The total average time was approximately 30 ms for all cases.

In case RF-1 (a) and RF-4 (c) in Figure 5.8, with adiabatic walls, the absence of heat loss allows the flame to anchor firmly at the sharp tip, producing a strong recirculation region of high temperature. Slight differences in the shape and size of the recirculation zone can be observed. In RF-4, the high temperature region is slightly more elongated and shifted downstream compared to the adiabatic, RF-1, case (a). This behavior highlights the influence of Reynolds number on the size and shape of the recirculation zone. Interestingly, the numerical prediction here contradict the experimental observations, which report an increase in recirculation zone size with increasing Reynolds number. One likely explanation is the limitation of the 2D simulations as the absence of 3D vortex dynamics, the flow physics governing the formation and stability of the trapped vortex cannot be fully captured. Additionally, when comparing case RF-4 with case RF-6 (d), the different liner boundary conditions are seen to result in a larger recirculation zone in case (d) with higher temperature downstream compared to case (c). The adiabatic cases systematically lead to overall lower temperature in the downstream portion of the combustor, which may indicate incomplete combustion and reduced system efficiency.

Case	**RF-1**	**RF-3**	**RF-4**	**RF-6**	**Cantera**
$T_{\max}$ (K)	1326.1	1314.2	1330.6	1349.6	981.06

Table 5.1: Peak temperature comparison between selected PeleLMeX cases and Cantera

Table 5.1, gives a comparison of peak instantaneous temperature for the four stable cases, with the adiabatic flame temperature computed in Cantera. The resulting temperature from Cantera corresponds to the theoretical adiabatic flame temperature for the specified equivalence ratio and inlet conditions. In, RF-1 we observe a higher temperature when compared to the same Reynolds number case (RF-3). This is most likely due to the fact that the flame in RF-3 gets dislocated and partially extinguished, even though it is able to revive itself, also the adiabatic wall in RF-1, does not allow any heat loss through the liner wall which may also be a reason for the higher temperature we observed. The reverse tendencies are observed at lower Reynolds numbers, which may be due to the fact that the turbulence is not strong enough to perturb the flame front, while the incoming slightly hotter fresh gases lead to higher flame temperatures.

RF-3 displays significantly lower maximum temperature than RF-6 (both are with the fitted temperature profile). When the flow becomes less turbulent, the flame is subjected to lower levels of strain, stretch, and turbulent fluctuations. Conversely, at higher Reynolds numbers, enhanced turbulent mixing, vortex shedding, and local flame deformation increase flame stretch, which broadens the reaction zone and lowers the peak temperature [48, 64].

Overall, the observed temperature distribution across the cases reflects the combined influence of wall thermal boundary conditions and Reynolds number dependent flame dynamics. Figure 5.9 shows spatial location of the peak instantaneous temperatures in the domain for RF-6. In all cases, the highest temperatures occur near the flame front within the recirculation zone, with RF-4 slightly more downstream compared to the other cases.

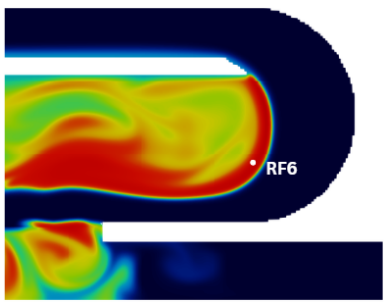

Figure 5.9: Peak instantaneous temperatures locations for reactive cases

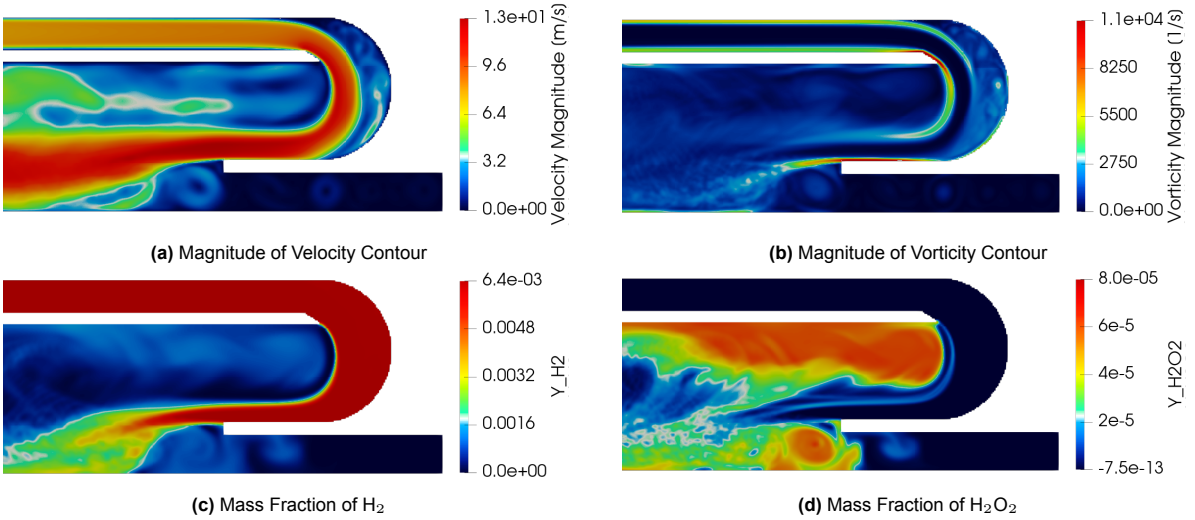

(a) Magnitude of Velocity Contour

(b) Magnitude of Vorticity Contour

(c) Mass Fraction of H_2

(d) Mass Fraction of H_2O_2

Figure 5.10: Results from RF-6

Figure 5.10 shows averaged velocity, heat release, H_2 and H_2O_2 mass fraction contours obtained from our RF-6 reactive simulation. The velocity contour (Figure 5.10a) qualitatively shows a similar flow pattern as the cold flow result as seen in figure 5.6a. The presence of a separation layer from the outer bend wall can clearly be seen. A high speed jet enters from the main inlet, accelerates around the bend, and generates a strong shear layer. However we do see a more uniform recirculation region as small scale vortices generated by the tip are not present in reactive case. Figure 5.10b shows the heat release field and highlights the location and intensity of chemical reactions. A thin, high magnitude reaction zone forms along the U bend, creating strong shear and ideal mixing with recirculated products. This region acts as the primary flame anchoring location, with peak heat release occurring at the tip that gradually decreases downstream.

The hydrogen mass fraction field (Figure 5.10c) locates the fuel path. Hydrogen enters the domain through the main inlet and remains concentrated near the U bend wall as it follows the curved geometry. Gruber et al. [35] and Hegde [36] also observed the same feature. Figure 5.10d shows hydrogen peroxide formation primarily in the low temperature region (see Figure 5.7f). Its distribution highlights low temperature chemistry is taking place, especially inside the trapped-vortex recirculation region. Overall, these four fields show how the flow, mixing, and chemistry interact.

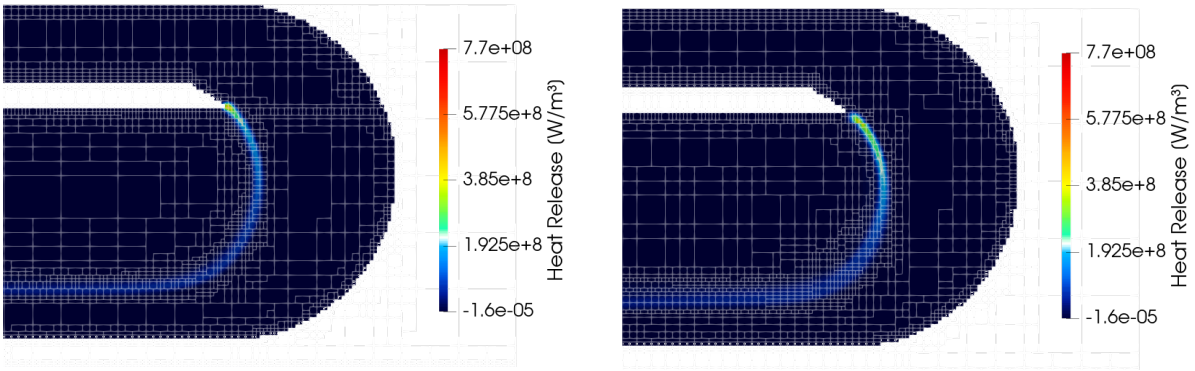

(a) RF-4

(b) RF-6

Figure 5.11: Averaged Heat release contours with overlaid AMR grid structure

5.2.3. Flame profiles

Figure 5.11 compares the heat release for RF-4 (adiabatic wall) and RF-6 (temperature-fitted wall), highlighting the effect of wall thermal boundary conditions on flame anchoring and local quenching. In RF-4, the adiabatic wall prevents any heat loss to the liner, representing an idealized first guess boundary condition, where the flame front remains attached to the sharp tip. In contrast, RF-6 uses a fitted wall temperature profile obtained from experiments, making it a more realistic representation. The spatially varying wall temperature causes heat losses near the tip, partially quenching the flame as it attempts to anchor. Flame quenching near the wall can weaken local stabilization, and in hydrogen based combustors this can promote flashback by allowing the reaction zone to propagate upstream.

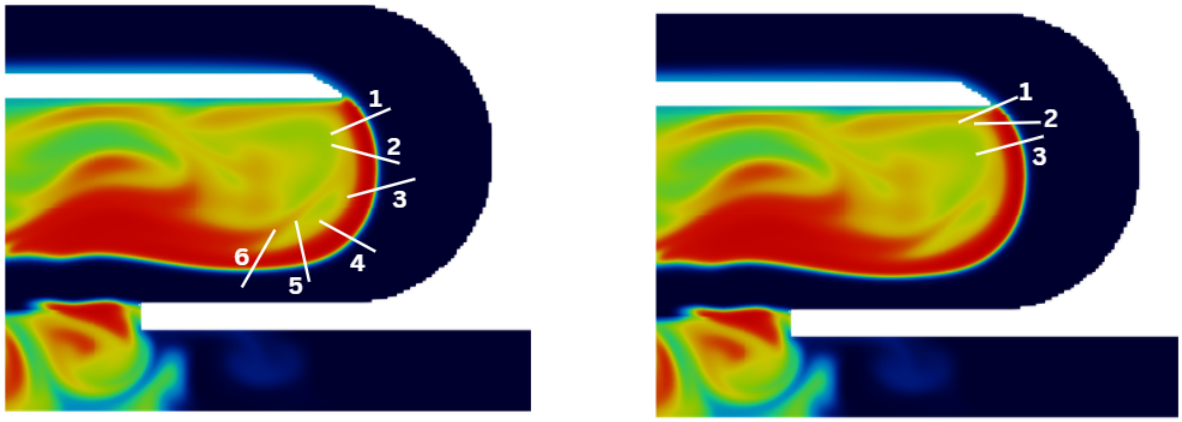

(a) **(b)**

Figure 5.12: 1D flame profiles, for analyzing H2 behavior accross the flame front in RF-4 and RF-6 (shown)

The mass fraction of H_2 and temperature along different profiles (Figure 5.12a) are shown in Figure 5.13 and Figure 5.14 for RF-4 and RF-6 cases respectively. The results are also compared to 1D flame from cantera. The CFD results in Figure 5.14a and Figure 5.13a reveal some deviations from the Cantera reference, H_2 concentration profiles have a slightly different slope. The flow field gets $180°$ inverted and organizes into a trapped vortex structure that substantially modifies the local flame behavior, an effect entirely absent in the 1D model. Additionally, from Figure 5.14b all CFD profiles exhibit higher peak temperatures than in Figure 5.13b and the Cantera solution, likely due to a locally elevated equivalence ratio, which effectively enriches the mixture locally.

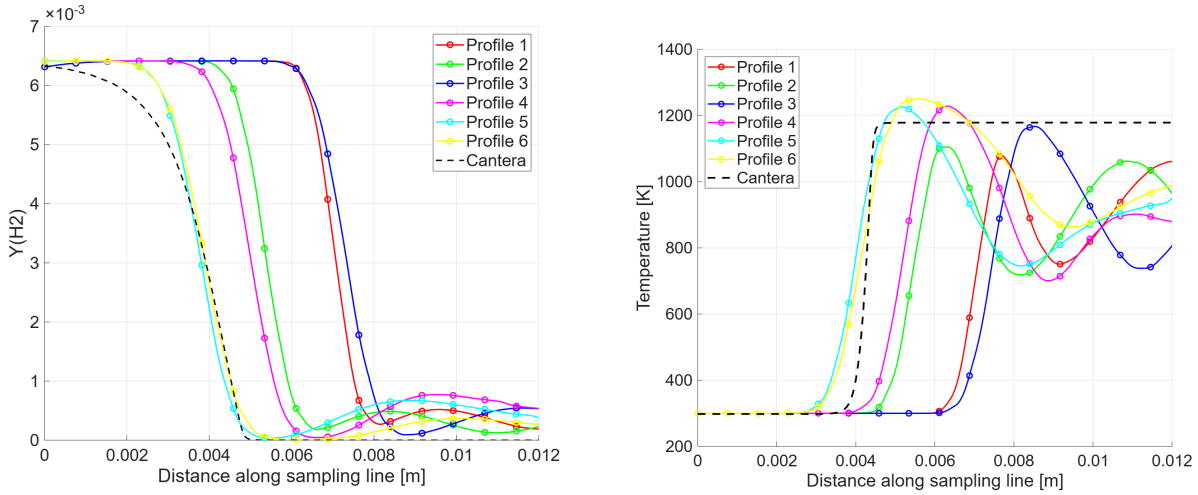

(a) (a) H2 mass fraction

(b) (b) Temperature

Figure 5.13: Comparison of H2 mass fraction and temperature along the curves shown in Figure 5.12a for RF-4

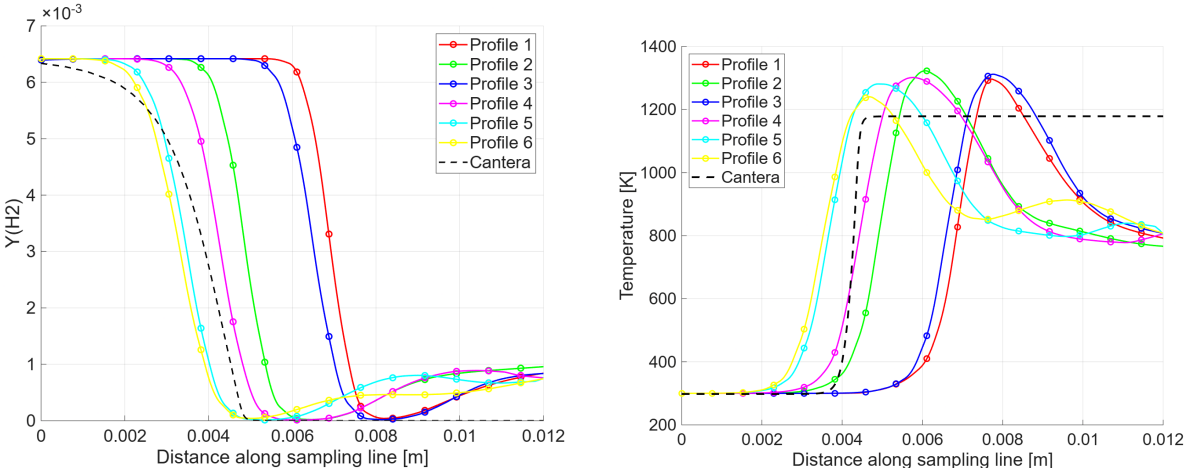

(a) (a) H2 mass fraction

(b) (b) Temperature

Figure 5.14: Comparison of H2 mass fraction and temperature along the curves shown in Figure 5.12a for RF-6

Figure 5.15, compares the temperature profiles as a function of hydrogen mass fraction for three lines near the tip (see Figure 5.12b), for two different cases: RF-4 (adiabatic) and RF-6 (isothermal F). The comparison of temperature profiles along three lines near the wall reveals a significant influence of wall boundary conditions on hydrogen combustion characteristics, with RF-6 consistently yielding higher gas temperatures than the adiabatic wall case (RF-4) across all profiles. This counter intuitive result suggests that wall heat transfer is not merely a loss mechanism but also modifies near wall combustion dynamics, potentially through enhanced reaction kinetics or improved local mixing induced by thermal gradients. Additionally, line 1 for RF-6 shows a big difference from its counterpart in RF-4, highlighting the influence of proper thermal BC. Further analysis might be required to understand this phenomenon better.

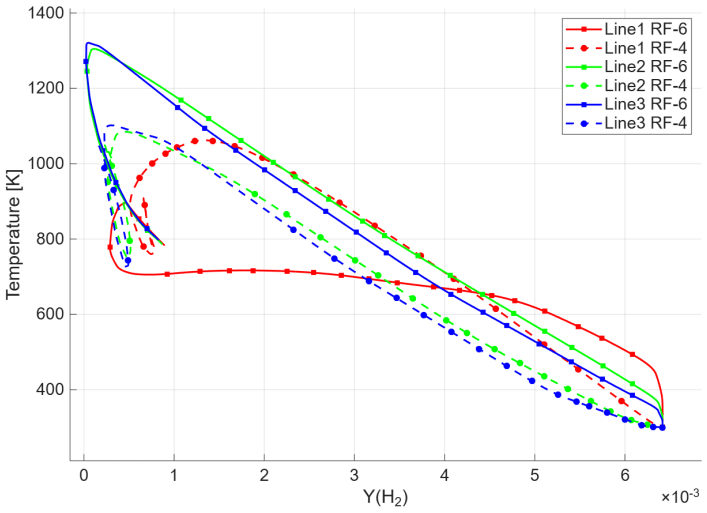

Figure 5.15: Profiles for analyzing H2 across the flame front

6

Conclusion and Recommendations

Hydrogen as a fuel has gained a lot of interest as it can act as a carbon free energy carrier in the global transition toward sustainable energy systems. But from our literature review, we can see that there are still challenges that needs to be overcome in order to use it safely in gas turbines. Accurate prediction and control of these phenomena require high fidelity modeling with realistic boundary conditions, which remains an ongoing challenge in computational combustion.

The main objective of this work was to get on step closer to the above mentioned objective, by investigating the influence of thermal wall BC on the flow and the structure of a well characterized lean premixed H_2 flame, using 2D quasi Direct Numerical Simulations. A simplified 2D representation of the FlameSheet™ burner was modeled using the PeleLMeX solver, with particular attention paid to the thermal treatment of the thin liner walls. Three thermal BCs were evaluated: 1) adiabatic, 2) isothermal at 300 K, and 3) a temperature fitted profile derived from experimental measurements. Simulations were conducted at two Reynolds numbers (12,000 and 8,000) under lean premixed conditions (equivalence ratio $\phi = 0.2$).

This chapter presents the research work done in this thesis and the key findings are summarized below with respect to the objectives outlined in section 1.4.

- What are the computational model requirements necessary to study the flame wall interactions in the trapped vortex burner?
  - An AMR approach with a refinement ratio of 2 between levels was implemented, triggered by magnitude of vorticity and temperature as well as refinements in proximity to embedded boundaries. Main flow features were well captured at AMR level 3, level 5 refinement was necessary to resolve near wall gradients and detailed flame wall interactions.
  - The LiDryer mechanism (9 species, 19 reactions) was chosen after validation against experimental laminar flame speed and ignition delay data using Cantera. Its offers a favorable balance between computational cost and accuracy.
  - DNS was employed with detailed finite rate chemistry via the LiDryer mechanism. This approach resolves all turbulent and chemical scales, enabling a direct investigation of flame wall interactions without subgrid combustion modeling assumptions.
- How do different thermal boundary conditions on the liner walls affect flame stability, recirculation zone size and shape in lean premixed hydrogen combustion?
  - The 2D simulations clearly demonstrated that the choice of wall thermal treatment determines whether the flame remains anchored or extinguishes. Two distinct regimes emerged, cases RF-2 and RF-5 with isothermal walls at 300 K resulted in complete flame extinction at both Reynolds numbers (12,000 and 8,000), as also seen by Gruber et al. [35].
  - Cases with adiabatic (RF-1, RF-4) and temperature fitted (RF-3, RF-6) walls maintained stable flames, confirming that sufficient near wall temperatures are essential for hydrogen

flame anchoring. The fitted temperature profile from experimental measurements yielded flame behavior that better represents real combustion systems. Notably, the RF-6 case (fitted BC at Re=8,000) produced the most stable and coherent flame structure among all simulations, with the flame remaining anchored at the tip while showing a slight but physically consistent degree of flame front quenching.

- Can a 2D simulation framework provide meaningful insights into flame wall interactions and flashback mechanisms compared to more expensive 3D simulations?
  - While 2D simulations offer computational efficiency, they fail to capture essential 3D turbulent mechanisms such as vortex stretching, energy cascade, and spanwise instabilities. This limitation is particularly significant for highly turbulent flows which leads to reduced turbulent dissipation, resulting in higher predicted velocities and temperatures compared to both experimental data and 3D simulations.
  - 2D DNS, while simplified, can qualitatively capture important flame wall interaction phenomena, including near wall quenching and the critical balance between heat release and wall heat loss. The ability of the solver to correctly predict flame extinction under excessive cooling conditions builds confidence in its application to more complex hydrogen combustion problems.

6.1. Limitations and Recommendations

While this study provided important insights, several limitations should be acknowledged:

- Dimensionality constraints: The 2D approach cannot capture 3D turbulent structures, vortex stretching, or out of plane instabilities that are present in real combustors. It is recommended to extend the analysis to 3D using LES or DNS to capture the full turbulent spectrum and validate the qualitative wall-effects trends observed in 2D.
- Simplified geometry: The 2D representation omits spanwise variations and 3D flow features that may affect flame stabilization.
- Modelling approach: Implementing two-way coupled heat transfer between fluid and solid domains could eliminate the need for prescribed thermal boundary conditions altogether.
- Limited flashback analysis: A dedicated parametric study should be conducted to systematically map flashback limits, and try to reproduce results obtained by Zeman and Pichler [85]. Simulations could be performed by progressively increasing Reynolds numbers until flashback occurs.

References

[1] U. Ahmed, S. P. Malkeson, A. L. Pillai, N. Chakraborty, and R. Kurose. “Flame self-interaction during turbulent boundary layer flashback of hydrogen-rich premixed combustion”. In: *Physical Review Fluids* 8.2 (Feb. 2023). ISSN: 2469-990X. DOI: 10.1103/physrevfluids.8.023202.

[2] Vladimir A. Alekseev, Moah Christensen, Edouard Berrocal, Elna J.K. Nilsson, and Alexander A. Konnov. “Laminar premixed flat non-stretched lean flames of hydrogen in air”. In: *Combustion and Flame* 162.10 (Oct. 2015), pp. 4063–4074. ISSN: 0010-2180. DOI: 10.1016/j.combustflame.2015.07.045.

[3] C. Altantzis, C.E. Frouzakis, A.G. Tomboulides, S.G. Kerkemeier, and K. Boulouchos. “Detailed numerical simulations of intrinsically unstable two-dimensional planar lean premixed hydrogen/air flames”. In: *Proceedings of the Combustion Institute* 33.1 (2011), pp. 1261–1268. ISSN: 1540-7489. DOI: 10.1016/j.proci.2010.06.082.

[4] L. A. Altenburg, S. A. Klein, and M. J. Tummers. “Flame stabilization and flashback pathways in a trapped vortex premixed hydrogen-air flame”. In preparation. 2025.

[5] M. M. Ameen and J. Abraham. “Are “2D DNS” results of turbulent fuel/air mixing layers useful for assessing subgrid-scale models?” In: *Numerical Heat Transfer, Part A: Applications* 69.1 (2015), pp. 1–13. ISSN: 1521-0634. DOI: 10.1080/10407782.2015.1052312.

[6] AMReX-Combustion Development Team. *AMReX-Combustion (GitHub repository)*. https://github.com/AMReX-Combustion. 2025.

[7] J. D. Anderson. “Ludwig Prandtl’s Boundary Layer”. In: *Physics Today* 58.12 (2005), pp. 42–48. ISSN: 1945-0699. DOI: 10.1063/1.2169443.

[8] ANSYS Inc. *ANSYS Fluent*. https://www.ansys.com/products/fluids/ansys-fluent. Version 2024R1. 2024.

[9] ANSYS Inc. *Species Transport and Finite-Rate Chemistry*. ANSYS Fluent Theory Guide. ENEA Neptunius Project. n.d. URL: https://www.afs.enea.it/project/neptunius/docs/fluent/html/th/node128.htm.

[10] A.J. Aspden, M.S. Day, and J.B. Bell. “Characterization of low Lewis number flames”. In: *Proceedings of the Combustion Institute* 33.1 (2011), pp. 1463–1471. ISSN: 1540-7489. DOI: 10.1016/j.proci.2010.05.090.

[11] G. Balakrishnan, M.D. Smooke, and F.A. Williams. “A numerical investigation of extinction and ignition limits in laminar nonpremixed counterflowing hydrogen-air streams for both elementary and reduced chemistry”. In: *Combustion and Flame* 102.3 (Aug. 1995), pp. 329–340. ISSN: 0010-2180. DOI: 10.1016/0010-2180(95)00031-z.

[12] A. C. Benim and K. J. Syed. *Flashback mechanisms in lean premixed gas turbine combustion*. Academic press, 2014.

[13] P. Boivin, C. Jiménez, A. L. Sánchez, and F. A. Williams. “An explicit reduced mechanism for H2–air combustion”. In: *Proceedings of the Combustion Institute* 33.1 (2011), pp. 517–523. DOI: 10.1016/j.proci.2010.05.002.

[14] T.D. Butler and P.J. O’Rourke. “A numerical method for two dimensional unsteady reacting flows”. In: *Symposium (International) on Combustion* 16.1 (Jan. 1977), pp. 1503–1515. ISSN: 0082-0784. DOI: 10.1016/s0082-0784(77)80432-3.

[15] Climate Action Tracker. *Warming Projections Global Update: December 2018 Briefing*. https://climateactiontracker.org/documents/507/CAT_2018-12-11_Briefing_WarmingProjectionsGlobalUpdate_Dec2018.pdf. Accessed: 2025-05-14. 2018.

[16] *Climate Change 2022 - Mitigation of Climate Change: Working Group III Contribution to the Sixth Assessment Report of the Intergovernmental Panel on Climate Change*. Cambridge University Press, July 2023. ISBN: 9781009157926. DOI: 10.1017/9781009157926.

[17] S. Daniele, P. Jansohn, and K. Boulouchos. “Flashback Propensity of Syngas Flames at High Pressure: Diagnostic and Control”. In: *Volume 2: Combustion, Fuels and Emissions, Parts A and B*. GT2010. ASMEDC, Oct. 2010, pp. 1169–1175. DOI: 10.1115/gt2010-23456.

[18] Marcus S Day and John B Bell. “Numerical simulation of laminar reacting flows with complex chemistry”. In: *Combustion Theory and Modelling* 4.4 (Dec. 2000). DOI: 10.1088/1364-7830/4/4/309.

[19] Z. Duan, B. Shaffer, and V. McDonell. “Study of Fuel Composition, Burner Material, and Tip Temperature Effects on Flashback of Enclosed Jet Flame”. In: *Journal of Engineering for Gas Turbines and Power* 135.12 (Sept. 2013). ISSN: 1528-8919. DOI: 10.1115/1.4025129.

[20] Z. Duan, B. Shaffer, V. McDonell, G. Baumgartner, and T. Sattelmayer. “Influence of Burner Material, Tip Temperature, and Geometrical Flame Configuration on Flashback Propensity of H2-Air Jet Flames”. In: *Journal of Engineering for Gas Turbines and Power* 136.2 (Oct. 2013). ISSN: 1528-8919. DOI: 10.1115/1.4025359.

[21] R. Edse. “Studies on burner flames of hydrogen-oxygen mixtures at high pressures”. In: *Wright Air Dev Cent Tech Rep* (1952), pp. 52–59.

[22] C. Eichler and T. Sattelmayer. “Premixed flame flashback in wall boundary layers studied by long-distance micro-PIV”. In: *Experiments in Fluids* 52.2 (2011), pp. 347–360. ISSN: 1432-1114. DOI: 10.1007/s00348-011-1226-8.

[23] A. Endres and T. Sattelmayer. “Large Eddy simulation of confined turbulent boundary layer flashback of premixed hydrogen-air flames”. In: *International Journal of Heat and Fluid Flow* 72 (Aug. 2018), pp. 151–160. ISSN: 0142-727X. DOI: 10.1016/j.ijheatfluidflow.2018.06.002.

[24] Lucas Esclapez et al. “PeleLMeX: an AMR Low Mach Number Reactive Flow Simulation Code without level sub-cycling”. In: *Journal of Open Source Software* 8.90 (Oct. 2023), p. 5450. ISSN: 2475-9066. DOI: 10.21105/joss.05450.

[25] Anne Felden. *Internal communication on 3D study of trapped vortex burner*. TU Delft. Unpublished. 2025.

[26] *FlameSheet™ for B- and E-Class*. https://thomassen.energy/retrofits-and-upgrades/flamesheet-for-b-and-e-class/. Accessed: 2025-12-05.

[27] Marc T. Henry de Frahan et al. “The Pele Simulation Suite for Reacting Flows at Exascale”. In: *Proceedings of the 2024 SIAM Conference on Parallel Processing for Scientific Computing (PP)*. Society for Industrial and Applied Mathematics, 2024, pp. 13–25. ISBN: 9781611977967. DOI: 10.1137/1.9781611977967.2.

[28] David J Gardner, Daniel R Reynolds, Carol S Woodward, and Cody J Balos. “Enabling new flexibility in the SUNDIALS suite of nonlinear and differential/algebraic equation solvers”. In: *ACM Transactions on Mathematical Software (TOMS)* 48.3 (2022), pp. 1–24. DOI: 10.1145/3539801.

[29] A. Giusti and E. Mastorakos. “Turbulent Combustion Modelling and Experiments: Recent Trends and Developments”. In: *Flow, Turbulence and Combustion* 103.4 (Nov. 2019), pp. 847–869. ISSN: 1573-1987. DOI: 10.1007/s10494-019-00072-6.

[30] L.P.H de Goey and J.H.M ten Thije Boonkkamp. “A flamelet description of premixed laminar flames and the relation with flame stretch”. In: *Combustion and Flame* 119.3 (Nov. 1999), pp. 253–271. ISSN: 0010-2180. DOI: 10.1016/s0010-2180(99)00052-8.

[31] A. D. F. Gonçalves. “Premixed hydrogen combustion: kinetic predictions of flame behaviour”. In: *Instituto Superior de Engenharia de Lisboa* (2022).

[32] David G. Goodwin, Harry K. Moffat, Ingmar Schoegl, Raymond L. Speth, and Bryan W. Weber. *Cantera: An Object-oriented Software Toolkit for Chemical Kinetics, Thermodynamics, and Transport Processes*. https://www.cantera.org. Version 3.2.0. 2025. DOI: 10.5281/zenodo.17620923.

[33] A. Gruber, J. H. Chen, D. Valiev, and C. K. Law. “Direct numerical simulation of premixed flame boundary layer flashback in turbulent channel flow”. In: *Journal of Fluid Mechanics* 709 (2012), pp. 516–542. ISSN: 1469-7645. DOI: 10.1017/jfm.2012.345.

[34] A. Gruber, A.R. Kerstein, D. Valiev, C.K. Law, H. Kolla, and J.H. Chen. “Modeling of mean flame shape during premixed flame flashback in turbulent boundary layers”. In: *Proceedings of the Combustion Institute* 35.2 (2015), pp. 1485–1492. ISSN: 1540-7489. DOI: 10.1016/j.proci.2014.06.073.

[35] Andrea Gruber, Tarjei Heggset, Ole Meyer, Luuk Altenburg, Mark Tummers, Sikke Klein, Joris Koomen, and Peter Stuttaford. “Numerical and Experimental Investigation of a Geometrically Simplified, Two-Dimensional FlameSheet™ Hydrogen Burner”. In: *Volume 3B: Combustion, Fuels, and Emissions*. GT2023. American Society of Mechanical Engineers, 2023. DOI: 10.1115/gt2023-103779.

[36] Tarun Hegde. “Numerical Investigations of a Trapped Vortex Hydrogen Burner”. MA thesis. Technische Universiteit Delft, 2024.

[37] Roy Hermanns. *The HELIOS project*. https://h2gt-helios.eu/. 2023.

[38] V. Hoferichter, C. Hirsch, T. Sattelmayer, A. Kalantari, E. Sullivan-Lewis, and Vincent McDonell. “Comparison of Two Methods to Predict Boundary Layer Flashback Limits of Turbulent Hydrogen-Air Jet Flames”. In: *Flow, Turbulence and Combustion* 100.3 (Dec. 2017), pp. 849–873. ISSN: 1573-1987. DOI: 10.1007/s10494-017-9882-2.

[39] Alireza Kalantari and Vincent McDonell. “Boundary layer flashback of non-swirling premixed flames: Mechanisms, fundamental research, and recent advances”. In: *Progress in Energy and Combustion Science* 61 (July 2017), pp. 249–292. ISSN: 0360-1285. DOI: 10.1016/j.pecs.2017.03.001.

[40] Alireza Kalantari, Elliot Sullivan-Lewis, and Vincent McDonell. “Application of a Turbulent Jet Flame Flashback Propensity Model to a Commercial Gas Turbine Combustor”. In: *Journal of Engineering for Gas Turbines and Power* 139.4 (Oct. 2016). ISSN: 1528-8919. DOI: 10.1115/1.4034649.

[41] Alireza Kalantari, Elliot Sullivan-Lewis, and Vincent McDonell. “Flashback Propensity of Turbulent Hydrogen–Air Jet Flames at Gas Turbine Premixer Conditions”. In: *Journal of Engineering for Gas Turbines and Power* 138.6 (Nov. 2015). ISSN: 1528-8919. DOI: 10.1115/1.4031761.

[42] Marco Konle, Frank Kiesewetter, and Thomas Sattelmayer. “Simultaneous high repetition rate PIV–LIF-measurements of CIVB driven flashback”. In: *Experiments in Fluids* 44.4 (2007), pp. 529–538. ISSN: 1432-1114. DOI: 10.1007/s00348-007-0411-2.

[43] Alexander A. Konnov. “Remaining uncertainties in the kinetic mechanism of hydrogen combustion”. In: *Combustion and Flame* 152.4 (Mar. 2008), pp. 507–528. ISSN: 0010-2180. DOI: 10.1016/j.combustflame.2007.10.024.

[44] Michael C. Krejci, Olivier Mathieu, Andrew J. Vissotski, Sankaranarayanan Ravi, Travis G. Sikes, Eric L. Petersen, Alan Kérmonès, Wayne Metcalfe, and Henry J. Curran. “Laminar Flame Speed and Ignition Delay Time Data for the Kinetic Modeling of Hydrogen and Syngas Fuel Blends”. In: *Journal of Engineering for Gas Turbines and Power* 135.2 (Jan. 2013). ISSN: 1528-8919. DOI: 10.1115/1.4007737.

[45] K.S.G. Krishnan, O. Bertram, and O. Seibel. “Review of hybrid laminar flow control systems”. In: *Progress in Aerospace Sciences* 93 (2017), pp. 24–52. ISSN: 0376-0421. DOI: 10.1016/j.paerosci.2017.05.005.

[46] P. K. Kundu, I. M. Cohen, and D. R. Dowling. *Fluid Mechanics*. 6th ed. Boston, MA: Academic Press, 2015. ISBN: 9780124059351.

[47] K. K. Kuo. *Principles of Combustion*. en. 2nd ed. Nashville, TN: John Wiley & Sons, Jan. 2005.

[48] C. K. Law. *Combustion physics*. Cambridge university press, 2010.

[49] C.K Law and C.J Sung. “Structure, aerodynamics, and geometry of premixed flamelets”. In: *Progress in Energy and Combustion Science* 26.4–6 (Aug. 2000), pp. 459–505. ISSN: 0360-1285. DOI: 10.1016/s0360-1285(00)00018-6. URL: http://dx.doi.org/10.1016/S0360-1285(00)00018-6.

[50] B. Lewis and G. von Elbe. “Stability and Structure of Burner Flames”. In: *The Journal of Chemical Physics* 11.2 (Feb. 1943), pp. 75–97. ISSN: 1089-7690. DOI: 10.1063/1.1723808.

[51] J. Li, Z. Zhao, A. Kazakov, and F. L. Dryer. “An updated comprehensive kinetic model of hydrogen combustion”. In: *International Journal of Chemical Kinetics* 36.10 (Aug. 2004), pp. 566–575. ISSN: 1097-4601. DOI: 10.1002/kin.20026.

[52] T. Lieuwen, V. McDonell, D. Santavicca, and T. Sattelmayer. “Burner Development and Operability Issues Associated with Steady Flowing Syngas Fired Combustors”. In: *Combustion Science and Technology* 180.6 (2008), pp. 1169–1192. ISSN: 1563-521X. DOI: 10.1080/00102200801963375.

[53] D O Lignell, J H Chen, and E S Richardson. “Terascale direct numerical simulations of turbulent combustion — fundamental understanding towards predictive models”. In: *Journal of Physics: Conference Series* 125 (July 2008), p. 012031. ISSN: 1742-6596. DOI: 10.1088/1742-6596/125/1/012031.

[54] W. Lubitz and W. Tumas. “Hydrogen: An Overview”. In: *Chemical Reviews* 107.10 (Oct. 2007), pp. 3900–3903. ISSN: 1520-6890. DOI: 10.1021/cr050200z. URL: http://dx.doi.org/10.1021/cr050200z.

[55] B. F. Magnussen. “The eddy dissipation concept: A bridge between science and technology”. In: *ECCOMAS thematic conference on computational combustion*. Vol. 21. Libson, Portugal. 2005, p. 24.

[56] H. J. Merk. “The macroscopic equations for simultaneous heat and mass transfer in isotropic, continuous and closed systems”. In: *Applied Scientific Research* 8.1 (1959), pp. 73–99. ISSN: 1573-1987. DOI: 10.1007/bf00411741.

[57] F. Nicoud and F. Ducros. “Subgrid-Scale Stress Modelling Based on the Square of the Velocity Gradient Tensor”. In: *Flow, Turbulence and Combustion* 62.3 (Sept. 1999), pp. 183–200. ISSN: 1573-1987. DOI: 10.1023/a:1009995426001. URL: http://dx.doi.org/10.1023/A:1009995426001.

[58] F. Nicoud, H. B. Toda, O. Cabrit, S. Bose, and J.I Lee. “Using singular values to build a subgrid-scale model for large eddy simulations”. In: *Physics of fluids* 23.8 (2011).

[59] A. Nonaka, M. S. Day, and J. B. Bell. “A conservative, thermodynamically consistent numerical approach for low Mach number combustion. Part I: Single-level integration”. In: *Combustion Theory and Modelling* 22.1 (2018), pp. 156–184.

[60] Andrew Nonaka, Yifei Sun, John Bell, and Aleksandar Donev. “Low Mach number fluctuating hydrodynamics of binary liquid mixtures”. In: *Communications in Applied Mathematics and Computational Science* 10.2 (2015), pp. 163–204.

[61] M. Ó Conaire, H. J. Curran, J. M. Simmie, W. J. Pitz, and C. K. Westbrook. “A comprehensive modeling study of hydrogen oxidation”. In: *International Journal of Chemical Kinetics* 36.11 (Aug. 2004), pp. 603–622. ISSN: 1097-4601. DOI: 10.1002/kin.20036.

[62] C. Olm, I. G. Zsély, R. Pálvölgyi, T. Varga, T. Nagy, H. J. Curran, and T. Turányi. “Comparison of the performance of several recent hydrogen combustion mechanisms”. In: *Combustion and Flame* 161.9 (Sept. 2014), pp. 2219–2234. ISSN: 0010-2180. DOI: 10.1016/j.combustflame.2014.03.006.

[63] N. Peters. “The turbulent burning velocity for large-scale and small-scale turbulence”. In: *Journal of Fluid Mechanics* 384 (1999), pp. 107–132. ISSN: 1469-7645. DOI: 10.1017/s0022112098004212.

[64] Thierry Poinsot and Denis Veynante. *Theoretical and Numerical Combustion*. 3rd ed. Philadelphia, PA: RT Edwards, 2012.

[65] Power Systems Mfg (PSM). *Flamesheet for E and F-Class Retrofits and Upgrades*. Accessed 2025. URL: https://www.psm.com/retrofits-and-upgrades/flamesheet-for-e-and-f-class.

[66] Exascale Computing Project. *Pele application suite*. Accessed: 2025-08-12. 2023. URL: https://www.exascaleproject.org/combustion-pele-a-new-exascale-capability-for-improving-engine-design/pele-application-suite/.

[67] O. Rathore and S. Navarro-Martinez. “Flame Dynamics Modelling Using Artificially Thickened Models”. In: *Flow, Turbulence and Combustion* 111.3 (June 2023), pp. 897–927. ISSN: 1573-1987. DOI: 10.1007/s10494-023-00433-2.

[68] W. Roquemore, D. Shouse, D. Burrus, A. Johnson, C. Cooper, B. Duncan, K.-Y. Hsu, V. Katta, G. Sturgess, and I. Vihinen. “Vortex combustor concept for gas turbine engines”. In: *39th Aerospace Sciences Meeting and Exhibit*. American Institute of Aeronautics and Astronautics, Jan. 2001. DOI: 10.2514/6.2001-483.

[69] B. Shadidi, G. Najafi, and T. Yusaf. “A Review of Hydrogen as a Fuel in Internal Combustion Engines”. In: *Energies* 14.19 (Sept. 2021). ISSN: 1996-1073. DOI: 10.3390/en14196209.

[70] R. Sharifzadeh and A. Afshari. “Assessment of a hydrogen-fueled swirling trapped-vortex combustor using large-eddy simulation”. In: *Fuel* 357 (Feb. 2024), p. 129847. ISSN: 0016-2361. DOI: 10.1016/j.fuel.2023.129847.

[71] Yasaman Shirian, Jeremy Horwitz, and Ali Mani. “On the convergence of statistics in simulations of stationary turbulent flows”. In: *arXiv preprint arXiv:2110.10300* (2021).

[72] J. Smagorinsky. “General circulation experiments with the primitive equations: I. The basic experiment”. In: *Monthly Weather Review* 91.3 (Mar. 1963), pp. 99–164. ISSN: 1520-0493. DOI: 10.1175/1520-0493(1963)091<0099:gcewtp>2.3.co;2. URL: http://dx.doi.org/10.1175/1520-0493(1963)091%3C0099:GCEWTP%3E2.3.CO;2.

[73] D. B. Spalding. “Development of the eddy-break-up model of turbulent combustion”. In: *Symposium (International) on Combustion*. Vol. 16. 1. Elsevier BV. 1977, pp. 1657–1663.

[74] P. Stuttaford and H. Rizkalla. “Flamesheet Combustor Contoured Liner”. en. US10,060,630 B2. United States Patent. Aug. 2018. URL: http://www.google.it/patents/US10060630.

[75] P. Stuttaford and H. Rizkalla. “Flamesheet combustor dome”. en. US9,752,781 B2. United States Patent. Aug. 2017. URL: http://www.google.it/patents/US9752781.

[76] Peter Stuttaford, Hany Rizkalla, Khalid Oumejjoud, Nicolas Demougeot, Justin Bosnoian, Fred Hernandez, Matthew Yaquinto, Afzal Pasha Mohammed, Dwain Terrell, and Ryan Weller. “FlameSheet™ Combustor Engine and Rig Validation for Operational and Fuel Flexibility With Low Emissions”. In: *Volume 4A: Combustion, Fuels and Emissions*. GT2016. American Society of Mechanical Engineers, 2016. DOI: 10.1115/gt2016-56696.

[77] AMReX Team. *Embedded boundaries*. Accessed: 2025-08-12. 2025. URL: https://amrex-codes.github.io/amrex/docs_html/EB_Chapter.html.

[78] U.S. Department of Energy. *COP28: Countries Launch Declaration of Intent on Clean Hydrogen*. https://www.energy.gov/articles/cop28-countries-launch-declaration-intent-clean-hydrogen. Accessed: 2025-05-14. 2023.

[79] United Nations Framework Convention on Climate Change. *COP28 agreement signals beginning of the end of the fossil fuel era*. https://unfccc.int/news/cop28-agreement-signals-beginning-of-the-end-of-the-fossil-fuel-era. Accessed: 2025-05-14. 2023.

[80] United Nations Framework Convention on Climate Change. *Paris Agreement*. https://unfccc.int/sites/default/files/english_paris_agreement.pdf. Accessed: 2025-05-14. 2015.

[81] M. R. Usman. “Hydrogen storage methods: Review and current status”. In: *Renewable and Sustainable Energy Reviews* 167 (Oct. 2022), p. 112743. ISSN: 1364-0321. DOI: 10.1016/j.rser.2022.112743. URL: http://dx.doi.org/10.1016/j.rser.2022.112743.

[82] J.A. Van Oijen and L.P.H. De Goey. “Modelling of premixed laminar flames using flamelet-generated manifolds”. In: *Combustion science and technology* 161.1 (2000), pp. 113–137.

[83] H. Versteeg and W. Malalasekera. *An introduction to computational fluid dynamics*. 2nd ed. Philadelphia, PA: Prentice Hall, Feb. 2007.

[84] M. Yue, Hugo Lambert, Elodie Pahon, Robin Roche, Samir Jemei, and Daniel Hissel. “Hydrogen energy systems: A critical review of technologies, applications, trends and challenges”. In: *Renewable and Sustainable Energy Reviews* 146 (Aug. 2021), p. 111180. ISSN: 1364-0321. DOI: 10.1016/j.rser.2021.111180. URL: http://dx.doi.org/10.1016/j.rser.2021.111180.

[85] A. Zeman. *Experimental Investigation of Hydrogen Combustion in a 2-D Trapped-Vortex Burner*. Master's thesis. Master's thesis. 2025. URL: https://resolver.tudelft.nl/uuid:5a0f00e6-fbf8-4350-93a1-14d4fcede50f.

[86] P. Zhang, I. G. Zsély, V. Samu, T. Nagy, and T. Turányi. "Comparison of Methane Combustion Mechanisms Using Shock Tube and Rapid Compression Machine Ignition Delay Time Measurements". In: *Energy amp; Fuels* 35.15 (July 2021), pp. 12329–12351. ISSN: 1520-5029. DOI: 10.1021/acs.energyfuels.0c04277.

[87] Weiqun Zhang, Ann Almgren, Vince Beckner, John Bell, Johannes Blaschke, Cy Chan, Marcus Day, Brian Friesen, Kevin Gott, Daniel Graves, et al. "AMReX: a framework for block-structured adaptive mesh refinement". In: *The Journal of Open Source Software* 4.37 (2019), p. 1370.

[88] J. Zips, C. Traxinger, P. Breda, and M. Pfitzner. "Assessment of presumed/transported probability density function methods for rocket combustion simulations". In: *Journal of Propulsion and Power* 35.4 (2019), pp. 747–764.